Comparison between eddy-covariance and flux-gradient size-resolved dust fluxes during wind erosion events

Sylvain Dupont, J.-l. Rajot, Eric Lamaud, G. Bergametti, M. Labiadh, B. Khalfallah, C. Bouet, B. Marticorena, R. Fernandes

JGR Atmospheres

RESEARCH ARTICLE
10.1029/2021JD034735

Comparison Between Eddy-Covariance and Flux-Gradient Size-Resolved Dust Fluxes During Wind Erosion Events

S. Dupont[1], J.-L. Rajot[2,3], E. Lamaud[1], G. Bergametti[3], M. Labiadh[4], B. Khalfallah[3], C. Bouet[2,3], B. Marticorena[3], and R. Fernandes[1]

[1]INRAE, Bordeaux Sciences Agro, ISPA, Villenave d'Ornon, France, [2]iEES Paris (Institut d'Ecologie et des Sciences de l'Environnement de Paris), UMR IRD 242, Université Paris Est Créteil - Sorbonne Université - CNRS - INRAE - Université de Paris, Bondy, France, [3]LISA (Laboratoire Interuniversitaire des Systèmes Atmosphériques), UMR CNRS 7583, Université Paris Est Créteil - Université de Paris, IPSL, Créteil, France, [4]IRA-Médenine, Médenine, Tunisia

Key Points:

- For the first time, the flux-gradient method used to estimate size-resolved dust fluxes is compared to the eddy-covariance method
- Both methods lead overall to similar dust fluxes. Differences are discussed, highlighting the difficulties and advantages of each method
- The EC method, rarely applied in aeolian soil erosion research, appears promising

Supporting Information:

Supporting Information may be found in the online version of this article.

Correspondence to:

S. Dupont,
sylvain.dupont@inrae.fr

Citation:

Dupont, S., Rajot, J.-L., Lamaud, E., Bergametti, G., Labiadh, M., Khalfallah, B., et al. (2021). Comparison between eddy-covariance and flux-gradient size-resolved dust fluxes during wind erosion events. *Journal of Geophysical Research: Atmospheres*, *126*, e2021JD034735. https://doi.org/10.1029/2021JD034735

Received 8 FEB 2021
Accepted 7 JUN 2021

Abstract Estimating accurately dust emission flux during aeolian erosion events is crucial for quantifying the amount of dust in the atmosphere. The rare existing field experiments quantifying such flux were mainly performed using the flux-gradient (FG) method. Here, we present the first intercomparison of the size-resolved dust fluxes estimated by both the FG and the eddy-covariance (EC) methods during several erosion events. Both methods were applied simultaneously during the WIND-O-V (WIND erOsion in presence of sparse Vegetation)'s 2017 field experiment over an isolated erodible bare plot in South Tunisia. Overall, both methods predict similar dust fluxes for particle smaller than about 4 μm. For coarser particles, the EC method predicts a smaller dust flux than the FG method. Factors explaining this difference are discussed such as the different sampling heads used by the dust particle counters of both methods, or the possible weakening of the constant dust flux layer at the location of the upper dust particle counter of the FG method. This intercomparison highlights the difficulties and advantages of each method as well as their complementarity.

1. Introduction

In situ measurements of dust emission flux during aeolian erosion events remain rare and challenging despite the environmental, climatic and health impacts of mineral dust in the atmosphere (Bonasoni et al., 2004; Derbyshire, 2007; Mahowald, 2011; Shao et al., 2011; Yin et al., 2002; Yu et al., 2015). Such measurements are particularly important for evaluating—improving dust emission schemes used in global and regional dust models. The observed poor performance of models in predicting dust suspension (Evan et al., 2014; Huneeus et al., 2011; Todd et al., 2008; Uno et al., 2006) is partly due to the lack of measurements of surface dust emission and deposition fluxes (Knippertz & Todd, 2012; Textor et al., 2006).

One difficulty of measuring dust emission flux is related to the large size distribution of dust particles, ranging from about 0.1 μm to more than 20 μm. This size range covers particles with different Stoke and drift numbers, that is, particles responding differently to the flow eddies and whose settling velocity becomes significant for the largest sizes compared to the main flow velocity scale (Shao, 2008). This broad range of dust particle sizes challenges the techniques required to estimate dust emission fluxes. In particular, the hypotheses or validity of the techniques are often limited to a certain particle size range, depending on the particle interactions-responses to turbulent motions or the amount of available dust particles. However, knowing the whole size distribution of the emitted dust is critical for estimating the dust impacts on different atmospheric components and processes such as radiation transfer through the atmosphere, cloud formation and biogeochemical cycles (e.g., Mahowald et al., 2014), which are particle size dependent. The emitted dust fluxes in particle size number and mass are consequently important.

The few field experiments measuring near-surface dust emission fluxes used exclusively the flux-gradient (FG) method (e.g., Gillette et al., 1972; Ishizuka et al., 2014; Nickling & Gillies, 1993; Shao et al., 2011; Sow et al., 2009). This method has the advantage of depending only on local mean quantities and thus do not require high frequency measurements. Only the measurements of the mean dust concentration at two levels and the mean wind velocity profile are needed. This method relies, however, on several hypotheses such as

a constant flux layer and the similarity in turbulent transport between dust and momentum, as reviewed in the next section. These hypotheses are rarely checked during erosion field experiments.

The eddy-covariance (EC) method represents an alternative to the FG method as it is a direct method to estimate dust fluxes without assumptions on eddy diffusion coefficients nor empirical constants to account for thermal stratification, as opposed to the FG method. Although the EC method is routinely used for estimating gas fluxes such as CO_2 and preferred to the FG method (e.g., Aubinet et al., 1999; Baldocchi, 2014), the EC method remains challenging for particle flux measurements. This is explained (a) by the difficulty of measuring simultaneously high frequency wind velocity components and particle concentration and (b) by the limitation of the EC method to assume that particles behave as gases, that is, passive particles following turbulent motions. For dust, this second point would correspond to particles smaller than 10 μm (Fratini et al., 2007). Larger particles (>10–20 μm) are not effortlessly carried by the turbulent eddies due to their inertia and gravity, a process known as particle trajectory crossing effect (e.g., Csanady, 1963; Fratini et al., 2007; Shao, 2008). Existing measurements on particle fluxes using the EC method were mainly performed over urban areas (e.g., Dorsey et al., 2002; Deventer, El-Madany, et al., 2015; Mårtensson et al., 2006), vegetated surfaces (e.g., Damay et al., 2009; Deventer, Held, et al., 2015), and much less over desert areas.

To our knowledge, only four field experiments have applied the EC technique to quantifying dust flux. In a pioneering experiment, Porch and Gillette (1977) estimated the dust flux using a vectorvane anemometer and a nephelometer, sampling dust concentration at 5 Hz. Their measurements were, however, limited to a dust deposition event with no distinction between particle sizes. Thirty years later, Fratini et al. (2007) estimated the size-resolved dust flux (from 0.26 to 7.00 μm in diameter) at 12 m above ground level (AGL) during erosion events in a desert region of Northern China. This represents the most detailed study of the EC method applied to dust fluxes. They used an ultrasonic anemometer and an optical particle counter (OPC) sampling dust at 5 Hz. More recently, Wang et al. (2017) presented an experiment on the dry lake bed of the Qingtu Lake in Western China with a vertical profile of 11 ultrasonic anemometers and OPCs, sampling dust at 1 Hz. Although they presented PM_{10} (Particulate Matter with aerodynamic diameter <10 μm) dust flux cospectra, their study focused only on the correlation between large-scale wind motions and dust concentration, without any detail on the application of the EC method. Finally, Dupont et al. (2019) analyzed size-resolved dust flux cospectra obtained at 3 m AGL in south Tunisia using an ultrasonic anemometer and an OPC sampling dust at 1 Hz. That study focused exclusively on the dissimilarity in turbulent transport between dust, heat, and momentum. None of the above studies compared the size-resolved dust fluxes obtained from EC and FG methods.

The goal of this study is to compare near-surface, size-resolved dust fluxes obtained from EC and FG methods during aeolian soil erosion events recorded during the WIND-O-V (WIND erOsion in presence of sparse Vegetation)'s 2017 field experiment (Dupont et al., 2018; Dupont et al., 2019). Although both approaches have been often compared for gases (e.g., Loubet et al., 2013), they have never been compared for dust particles. A comparison of methods is important in order to (a) investigate the potential of the EC approach for estimating dust flux as an alternative/complementary method to the FG approach traditionally used by the aeolian erosion community and (b) to evaluate the conditions of applicability of the FG method in regards to its underlying hypotheses.

2. Background

Vertical dust flux within the atmospheric surface boundary layer results from the vertical transport by turbulence of dust emitted (or depositing) at the surface. This turbulent transport is often assumed to be similar to the momentum transfer (Gillette et al., 1972). During wind erosion events, the near-surface turbulence (few meters above the ground) responsible for the transport of dust and momentum is mainly produced mechanically by the wind shear induced by surface friction. This near-surface turbulence exhibits a large range of eddy-scales, some of them transporting momentum and dust. These later active eddies are usually in contact with the surface where momentum absorption and dust emission occur, and scale with the distance from the ground. Estimating the dust and momentum fluxes requires quantifying the net amount of momentum and dust, respectively, transported vertically by these active eddies.

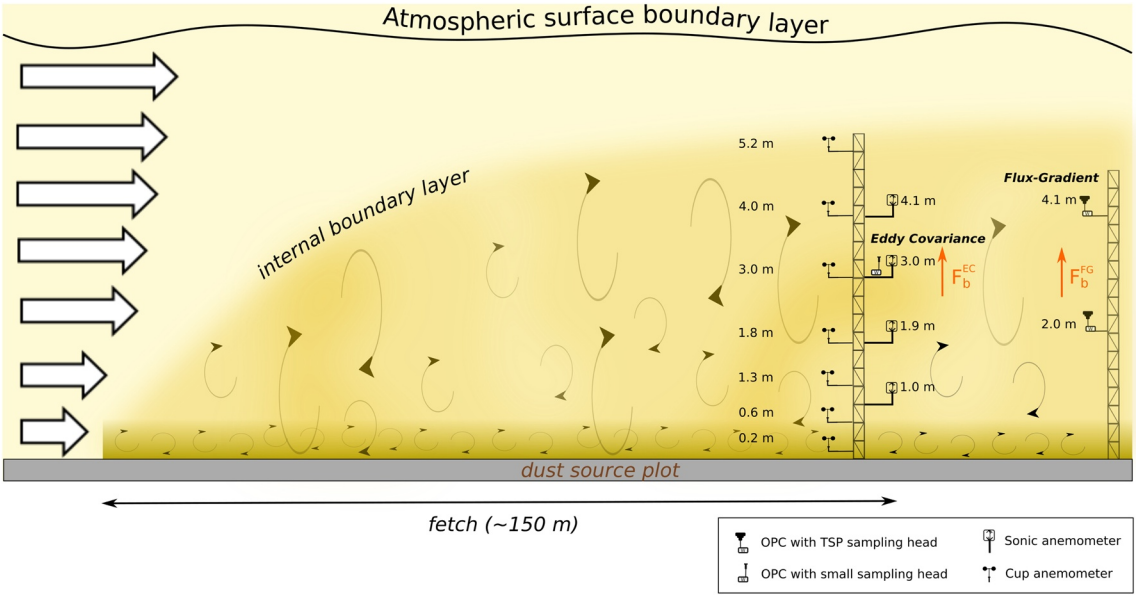

Figure 1. Schematic representation of the intercomparison between eddy-covariance (EC) and flux-gradient (FG) dust fluxes performed on an isolated erodible plot during the WIND-O-V's 2017 field experiment in Tunisia. F_b^{FG} and F_b^{EC} represent the FG and the EC size-resolved dust fluxes, respectively.

2.1. Constant Flux Layer

Due to the difficulty of measuring directly dust emission and momentum absorption at the surface, dust and momentum fluxes are usually measured at a few meter height above the surface, and then related to the surface fluxes by assuming a constant flux layer between the surface and the measurement height. This constant flux layer hypothesis is theoretically valid under horizontally homogeneous surface conditions and steady state conditions. In such conditions $\left(\partial\langle\rangle/\partial x = \partial\langle\rangle/\partial y = \partial\langle\rangle/\partial t = 0\right)$, the Navier Stokes and dust advection-diffusion equations simplify to, respectively:

$$\frac{\partial\langle u'w'\rangle}{\partial z} = 0 \quad \text{and} \quad \frac{\partial}{\partial z}\left(\langle w'd_b'\rangle - v_{s,b}\langle d_b\rangle\right) = 0, \tag{1}$$

where t is time; x, y and z are the streamwise, spanwise and vertical coordinates, respectively; u and w are the streamwise and vertical wind velocity components; d_b is the dust concentration in the air of the particle size bin b; and $v_{s,b}$ is the particle settling velocity. In Equation 1, a Reynolds decomposition of the variables has been applied such that $\alpha = \alpha + \alpha'$, where the symbol $\langle\ \rangle$ denotes the time average and the prime the deviation from the averaged value. The dust flux includes both the turbulent-diffusive flux ($\langle w'd_b'\rangle$) and the gravitational-settling flux ($v_{s,b}\langle d_b\rangle$). For mineral dust particle smaller than 10 μm in diameter, the gravitational-settling flux can be neglected (Fratini et al., 2007). Hence, under this constant flux layer condition and for dust particles <10 μm diameter, the measured turbulent-diffusive dust flux at a few meters above the surface is equal to the net dust flux at the surface (emission + deposition).

In field experiments, dust flux measurements are often performed over plots of a finite size. This is particularly true in semiarid regions where surfaces of different roughness and erodibility are juxtaposed as a consequence of human land use exploitation. In such a case, internal boundary layers develop from the upwind edges of plots due to differences of surface roughness and/or erodibility (Pendergrass & Arya, 1984) (Figure 1). Importantly, these internal boundary layers can differ in depth between momentum and dust. The flow and scalar fields adjust within the equilibrium sublayer of the internal layers with the plot surface characteristics. This equilibrium sublayer represents approximately the lowest 10% of the internal boundary layer where a constant momentum and scalar flux layer is achieved (Garratt, 1990; Kaimal & Finnigan, 1994). Above this level, the internal boundary layer corresponds to a sublayer transitioning with the upwind flow characteristics. The distance between the measurement location and the upwind edge is known as the fetch length. To relate the measured near-surface dust flux to the emitted dust flux from the

surface beneath, EC and FG measurements have to be located within the equilibrium sublayer where a constant dust flux layer is achieved.

2.2. Size-Resolved Flux-Gradient Dust Flux

The FG approach assumes proportionality between the vertical turbulent dust flux and the vertical gradient of the local mean dust concentration by analogy with the Fick's law for molecular diffusion. Hence, under negligible thermal stratification (neutral condition), the FG turbulent dust flux (F_b^{FG}) is expressed as:

$$F_b^{FG} = -K_{d,b}\frac{\partial\langle d_b\rangle}{\partial z}, \tag{2}$$

where $K_{d,b}$ is the dust eddy diffusion coefficient, which only depends on local mean quantities.

This phenomenological representation of turbulent fluxes means that the dominant eddies transferring dust vertically have much smaller time scale than the time scale over which the mean vertical dust gradient changes appreciably (Corrsin, 1975; Raupach & Legg, 1984). Hence, the dust transfer rate depends on the turnover eddy velocity and size, and is represented through $K_{d,b}$ while the dust exchange at height z is represented by the gradient $\partial\langle d_b\rangle$ / ∂z.

Following the Monin-Obukhov similarity theory (Monin & Obukhov, 1954), the effect of thermal stratification is only considered through the adjustment of the dust eddy diffusivity:

$$F_b^{FG} = -\frac{K_{d,b}}{\phi_d(\zeta)}\frac{\partial\langle d_b\rangle}{\partial z}, \tag{3}$$

where $\zeta = z/L$ is the atmospheric stability parameter, L the Obukhov length that compares the turbulence generated by buoyancy and wind shear, and ϕ_d the similarity function for dust accounting for the stability effect, determined empirically from experiments.

Similarly, the momentum flux can be expressed as:

$$\langle u'w'\rangle = -\frac{K_u}{\phi_u(\zeta)}\frac{\partial\langle u\rangle}{\partial z}, \tag{4}$$

where K_u is the momentum eddy diffusion coefficient and ϕ_u is the similarity function for momentum. Equation 4 leads to the well-known pseudo-logarithmic form of the mean velocity profile:

$$\langle u\rangle = \frac{u_{*0}}{\kappa}\left[\log\left(\frac{z}{z_0}\right) - \Psi_m\left(\frac{z}{L}\right) + \Psi_m\left(\frac{z_0}{L}\right)\right], \tag{5}$$

where u_{*0} is the friction velocity at the surface, Ψ_m the stability function accounting for the thermal stratification of the surface layer (e.g., Högström, 1988), κ the von Karman constant, and z_0 the roughness length. During wind erosion, (a) u_{*0} accounts for both surface wind shear and momentum flux absorbed by near-surface saltating particles (e.g., Raupach, 1991) and (b) z_0 is known as the saltation roughness length, integrating the surface roughness length and the additional roughness induced by saltating particles (Gillette et al., 1998; Owen, 1964; Raupach, 1991).

The dust eddy diffusion coefficient $K_{d,b}$ at the location of the flux is estimated from the momentum eddy diffusion coefficient such as $K_{d,b} = K_u/\mathrm{Sc}_t$, where Sc_t is the turbulent Schmidt number. Combining Equations 3 and 4 leads to:

$$F_b^{FG} = \frac{1}{\mathrm{Sc}_t}\frac{\phi_u(\zeta)}{\phi_d(\zeta)}u'w'\frac{\partial\langle d_b\rangle}{\partial\langle u\rangle}. \tag{6}$$

It is commonly assumed that momentum and dust particle eddy diffusivities are similar in three-dimensional homogeneous turbulence for particle diameters smaller than 10–20 μm, the particle trajectory crossing effect being negligible (Fratini et al., 2007; Shao, 2008). This leads to $\mathrm{Sc}_t = 1$ and $\phi_u = \phi_d$.

The simultaneous measurements of the dust concentration at two heights (z_{down} and z_{up}) and of the wind velocity profile, lead to the FG dust flux at height z_m ($= \sqrt{z_{down} z_{up}}$, geometric mean of z_{down} and z_{up}):

$$F_b^{FG} = \frac{\kappa}{u_{*0}} \langle u'w' \rangle_{z_m} \frac{\langle d_b \rangle_{z_{up}} - \langle d_b \rangle_{z_{down}}}{\log\left(z_{up} / z_{down}\right) - \Psi_m\left(z_{up} / L\right) + \Psi_m\left(z_{down} / L\right)}, \tag{7}$$

where $\langle u'w' \rangle_{z_m}$ is the momentum flux at height z_m.

Previous estimations of the dust flux using the FG method further assumed a constant momentum flux layer, that is, $\langle u'w' \rangle_{z_m} = -u_{*0}^2$, leading to (e.g., Sow et al., 2009):

$$F_b^{FG} = -\kappa u_{*0} \frac{\langle d_b \rangle_{z_{up}} - \langle d_b \rangle_{z_{down}}}{\log\left(z_{up} / z_{down}\right) - \Psi_m\left(z_{up} / L\right) + \Psi_m\left(z_{down} / L\right)}. \tag{8}$$

In Equation 8, u_{*0} and L are usually estimated using an iterative fitting procedure of the mean wind velocity and air temperature profiles predicted by Monin-Obukhov similarity theory (e.g., Frangi & Richard, 2000; Ishizuka et al., 2014; Marticorena et al., 2006).

In summary, the FG method relies on several hypotheses. First, the characteristic scale of the transporting mechanism must be small compared to the scale over which the mean gradient of the transported property changes appreciably (Corrsin, 1975; Raupach & Legg, 1984). Second, the turbulent dust transport is assumed similar to the momentum transport, leading to $\mathrm{Sc}_t = 1$ and $\phi_u = \phi_d$. Third, the local friction velocity is identical to the surface friction velocity (Equation 8), that is, assuming the presence of a perfect constant momentum flux layer. Fourth, both levels of dust measurements are located in a fully adjusted boundary layer (large uniform fetch) over an homogeneous terrain ($\partial\langle\rangle / \partial x = \partial\langle\rangle / \partial y = 0$). Fifth, the flow is stationary ($\partial\langle\rangle / \partial t = 0$).

2.3. Size-Resolved Eddy-Covariance Dust Flux

The EC approach is a direct method for estimating turbulent fluxes of scalars. The EC method requires calculating the correlation $\langle w'_{d,b} d'_b \rangle$ between the fluctuations of the dust concentration d'_b and the particle's vertical velocity $w'_{d,b}$. In other terms, it quantifies the balance between dust particles moving upward and downward, weighted by the particle's vertical velocity. For small mineral dust (<10 μm), particles can be assumed to behave like gases, and thus their velocity is considered equivalent to the flow velocity (Fratini et al., 2007). This leads to the EC dust flux:

$$F_b^{EC} = \langle w' d'_b \rangle. \tag{9}$$

Despite its direct approach, the EC method is difficult to implement. It requires the measurement of the wind vertical velocity component and dust concentration at the same location and at high frequency in order to capture all eddies transporting dust. Due to the difficulty of satisfying all these requirements, some corrections are often applied to the calculated EC flux (e.g., Foken, 2017).

To verify that the contribution to the flux of high frequency eddies have been included in the flux calculation, the cospectrum $S_{wd,b}$ of the flux has to be checked, the flux being equal to the integral over frequency of the cospectrum: $F_b^{EC} = \int_0^\infty S_{wd,b}\left(f\right) df$. Any high frequency loss or attenuation of the cospectrum is often the signature of low frequency measurements, meaning that the flux carried by the high frequency eddies has not been well captured. Fortunately, the cospectra of scalar (heat, gas, particles) and momentum fluxes often exhibit a similar well-known shape. Hence, the high frequency losses of the flux can be estimated by either using a shape model of the cospectrum available in the literature (e.g., Horst, 1997) or by fitting the

cospectrum curve with that of another scalar measured at higher frequency (e.g., Damay et al., 2009). This correction is only pertinent if most of the flux has been initially captured, that is, the peak of the cospectrum has been attained.

To verify that the sampling time is long enough to capture the low frequency component of the flux, an ogive analysis is usually done. This consists of tracing the cumulative integral of the flux cospectrum, starting from the highest frequencies. The ogive needs to converge to an asymptote at low frequencies (Oncley et al., 1996).

Steady state conditions are also required in order to satisfy the Reynolds decomposition postulates. Non-stationarity most often results from mesoscale variability of the flow, resulting in a trend in the time series with wavelength larger than the length of the time series. Before performing eddy-correlation calculations, these large-scale wavelengths with periods longer than 1/3 to 1/5 of the length of the series can be removed using linear or polynomial detrending techniques (Stull, 1988).

In summary, the EC method relies on only one hypothesis, a steady state condition, but the method is limited to dust particles <10 μm diameter. Its applicability requires high frequency measurements of both wind velocity and dust concentration, and a close positioning between the anemometer and the dust sensor. Failure to meet these constraints will require corrections to the flux.

2.4. Total Dust Flux

Independent of the technique used to estimate the size-resolved dust flux, the total dust flux, including all particle sizes, is computed in number and in mass, respectively, as follows:

$$F_{n,tot}^{\varphi} = \sum_{b}\left(\frac{dF_{b}^{\varphi}}{d\log\left(d_{p}\right)}\right)d\log\left(d_{p}\right), \tag{10}$$

$$F_{m,tot}^{\varphi} = \sum_{b}\left(\frac{dF_{b}^{\varphi}}{d\log\left(d_{p}\right)}\right)\rho_{p}\pi\frac{d_{p,b}^{3}}{6}d\log\left(d_{p}\right), \tag{11}$$

where φ is either FG or EC, d_p is the particle diameter, ρ_p is the dust mass density, and the subscripts n and m refer to number and mass, respectively. Although dust particles usually have a non-spherical shape (e.g., Chou et al., 2008), they are assumed spherical in Equation 11 as commonly adopted.

3. Materials and Methods

The WIND-O-V's 2017 field experiment was largely described in Dupont et al. (2018), Dupont et al. (2019), Khalfallah et al. (2020), and Dupont (2020), we only present here an overview.

3.1. Experimental Site

The experiment took place in south Tunisia, in the experimental range (Dar Dhaoui) of the Institut des Régions Arides (IRA) of Médenine. The plot approximates a flat half-circle of 150 m radius where measurements were performed at the center of the circle in order to ensure a fetch of at least 150 m for westerly, northerly to easterly winds (Figure 2a). In the north, the fetch was slightly longer, about 200 m. The area was characterized by a flat bare surface, surrounded by less erodible surfaces with small bushes in the northwest (0.34 ± 0.08 m height and 0.58 ± 0.20 m diameter) and young olive trees arranged in a square pattern in the northeast (about 1.7 ± 0.3 m height, 1.5 ± 0.4 m diameter, and 26 m spaced). Before the experiment and after the main rainfall events, the surface was tilled with a disc plow and leveled with a board in order to meet the conditions of an ideal flat bare soil without soil crust nor ridges.

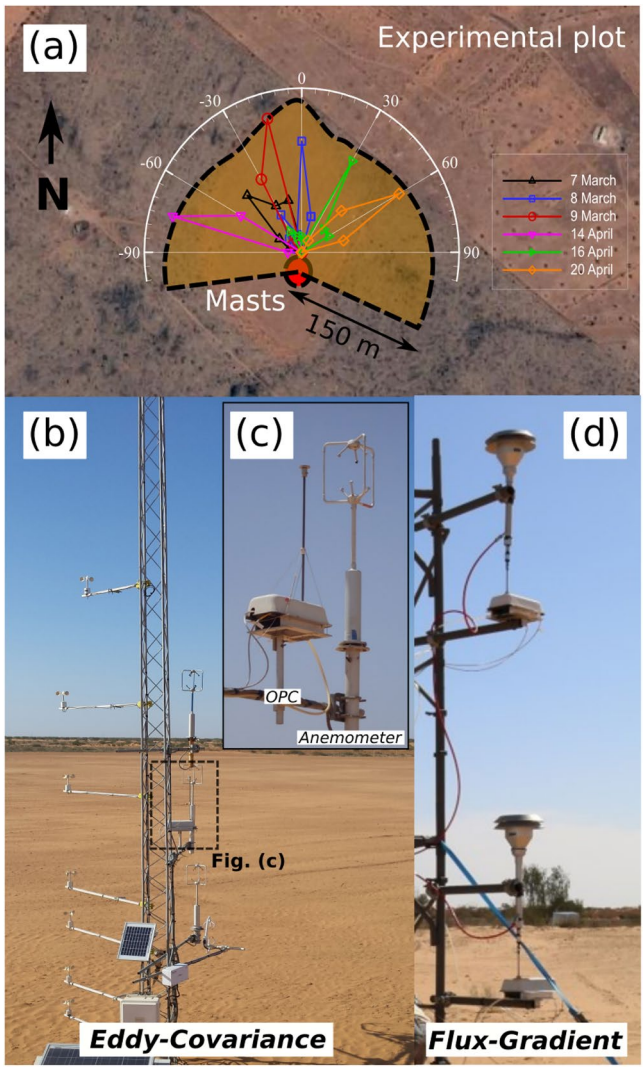

Figure 2. WIND-O-V's 2017 experiment. (a) Schematic representation of the near-half-circle experimental plot (dotted line) where the surface was tilled with a disc plow and leveled with a board in order to meet the conditions of an ideal flat bare soil without soil crust nor ridges. The measurement masts were located at its center. The wind roses indicate the main wind directions during the six erosion events. (b and c) North view of the plot from the back of the mast where cup and ultrasonic anemometers were mounted with a focus in (c) on the EC dust flux device composed of an OPC with a small sampling head located downwind of the 3 m high ultrasonic anemometer. (d) View of the two OPCs with their TSP sampling heads used for estimating the FG dust flux.

Our analysis focuses on six wind erosion events: 7-9 March 2017, and 14, 16 and 20 April 2017 (Table 1), whose meteorological and dust concentration characteristics were presented in Dupont et al. (2019), and for which dust emission resulted from saltation bombardment. These events occurred during daytime with different wind directions: west for the 14 April event, northwest for the 7-9 March events, northeast for the 20 April event, and northwest to northeast during the 16 April event. The 7 March and 14 April events had the lowest wind intensity, and thus, the lowest dust concentration. The 8 March event had the strongest wind peak, followed by the 16 April event. The 9 March and 20 April, events represent the best erosion events in terms of intensity, duration and stationarity. An intense rain event occurred between April 9 and 10, that is, before the three April wind events, with a cumulative rain amount of approximately 30 mm.

3.2. Meteorological Data Set

A 9 m high mast was erected at the center of the half-circle plot (Figure 2b). On this mast, turbulent velocity components (u, v, w) and air temperature (θ) fluctuations were measured simultaneously at 1.0, 1.9, 3.0, and 4.1 m AGL using 3D ultra sonic anemometers (one Campbell® Scientific CSAT3, two Gill R3, and one Gill WindMaster) sampling at 60, 50, 50, and 20 Hz, respectively. On the same mast, 7 cup anemometers (A100R Vector Instrument® at 0.2, 0.6, 1.3, 1.8, 3.0, 4.0, 5.2 m AGL) and 4 thermocouples (type T cupper/Constantan at 0.4, 1.6, 3.7, 5.0 m AGL) were also installed to measure simultaneously at 0.1 Hz the mean horizontal wind velocity and temperature profiles, respectively. All anemometers on the tower were intercalibrated prior to the experiment. Instruments installed on this mast are sketched in Figure 1.

A 15-min averaging time was chosen for computing wind statistics, as deduced from an ogive analysis (see Dupont et al., 2018). The wind velocity components recorded from the sonic anemometers were rotated so that u represents the horizontal component along the mean wind direction x, v the horizontal component along the transverse direction y, and w the vertical component. Prior to Reynolds decomposition of u, the large-scale trend with period larger than 15-min was simply removed from a sixth-order polynomial fit. Flow steadiness was tested for each 15-min period using the criterion given by Foken et al. (2004) in order to verify the low impact of mesoscale variability on the 15-min averaging periods.

The wind dynamics of the erosion events were previously analyzed in Dupont et al. (2018) and Dupont et al. (2019). The wind was found consistent with usual observations in surface boundary layer in terms of mean turbulent velocity profiles and main turbulent structures. A slight increase of the momentum flux at the top of the profile (4 m height) was observed during some events (see Figure S1), which may suggest a possible contamination of the top of the profiles by turbulence established with the rougher upwind surface outside the plot, although the mean velocity profile was well approximated by a logarithmic function. This will be further discussed in Sections 5.1 and 5.2.

Table 1
Main Characteristics of the Selected Wind Events: Surface Friction Velocity Deduced From the EC Approach (u_{*0}), Wind Direction (Wind Dir.), Stability (z/L), Number of 15-Min Time Periods During the Event (Nb 15-Min), Mean FG Total Dust Flux in Number ($F^{FG}_{n,tot}$) and in Mass ($F^{FG}_{m,tot}$)

Events	u_{*0} (ms^{-1})	wind dir. (°)	z/L	Nb 15-min	$F^{FG}_{n,tot}$(×10^7 #m^{-2}s^{-1})	$F^{FG}_{m,tot}$ (μgm^{-2}s^{-1})
7 March	0.30 (±0.04)	318 (±18)	−0.13 (±0.14)	40	1.0 (3.8)	320 (1,280)
8 March	0.32 (±0.09)	337 (±18)	−0.04 (±0.05)	32	2.1 (10.0)	710 (4,270)
9 March	0.35 (±0.05)	330 (±9)	−0.06 (±0.04)	40	2.2 (6.4)	770 (2,280)
14 April	0.29 (±0.03)	281 (±5)	−0.10 (±0.04)	26	1.0 (3.5)	190 (880)
16 April	0.33 (±0.06)	16 (±27)	−0.10 (±0.05)	30	2.5 (8.9)	830 (4,200)
20 April	0.32 (±0.06)	50 (±11)	−0.07 (±0.05)	53	1.8 (4.6)	390 (1,180)

Note. The mass fluxes were computed considering a mass density $\rho_p = 2{,}380\,\mathrm{kgm}^{-3}$ (Khalfallah et al., 2020). Between parentheses are indicated the standard deviations, except for the dust fluxes where it is the maximum flux.

3.3. FG Dust Flux

Two OPCs (PALAS, PROMO 2000 equipped with the aerosol sensor WELAS 2300 system) were installed on a scaffolding at $z_{down} = 2.0$ m and $z_{up} = 4.1$ m AGL, nearby the mast, to measure airborne dust concentration per size class at 1 Hz (Figures 1 and 2d). Both OPCs were equipped with a standard Total Suspended Particles (TSP) sampling head (BGI by Mesa Labs, Butler, NJ USA), commonly used in air quality measurements.

The two OPCs covered 0.3–17 μm diameter range particles, with 16 intervals per decade, leading to 28 size classes (bins). They measured the size and number of particles in sampled air in the optical chamber, delivered by a pump with a flow rate of 5 l min^{-1}. To ensure an isokinetic flow from the outside OPC inlet to the inside, the nominal flowrate of the TSP inlet was set to 16.7 l min^{-1}. Hence, this flow was isokinetically split in two: a main flow immediately directed to the OPC through a short vertical tube to minimize particle loss before measurement, and an auxiliary flow (11.7 l min^{-1}) controlled by an automated volumetric flow controller (MCR-50SLPM, Alicat Scientific). To improve the statistics of each bins, size-resolved dust concentration was synthesized in 14 bins between 0.3 and 17 μm by aggregating by two the intervals of the particle spectrometer and by removing the first interval, which is insufficiently accurate following the claim of the company. Before the experiment, the OPCs were calibrated using monodisperse dust particles of silicon dioxide (1.28 μm in diameter) as recommended by the manufacturer. Equivalence between the refractive indices of silicon dioxide and mineral dust particles was assumed.

At the end of the experiment, the two OPCs were installed at the same height for comparison. As described in Khalfallah et al. (2020), a correction was estimated for both OPCs in order to minimize differences in dust concentration measurements between both OPCs (Figure 3a), which is important when considering the difference of concentrations between both OPCs for estimating the FG dust flux. This correction was obtained with a good coefficient of determination ($R^2 > 0.95$) up to 9 μm (Figure 3b). Above 9 μm, a correction could not be evaluated due to the too low dust number concentration. Size classes above 9 μm were therefore discarded in our analysis. After correction, the remaining scatter (standard deviation) of the difference $D\langle d_b^{FG}\rangle$ between the two corrected OPC dust concentrations allowed us to evaluate the uncertainty on $D\langle d_b^{FG}\rangle$ relative to the mean dust concentration ($\Delta\left[D\langle d_b^{FG}\rangle\right]$ in Figure 3c). This uncertainty increases with particle size, and becomes significant for coarse particles due to their low concentration during the intercomparison campaign. This led us to approximate a threshold dust concentration difference $D\langle d_b^{FG}\rangle$ of 23% in each size class above which the difference between the dust concentrations measured by both OPCs in the gradient position can be considered significantly different.

The 15-min averaged dust flux F_b^{FG} was estimated per size class (bin) from the traditional approach used by the erosion community, assuming a constant momentum flux layer (Equation 8), and u_{*0} and L were calculated using an iterative fitting procedure of the mean wind velocity and air temperature profiles predicted by the Monin-Obukhov similarity theory (e.g., Frangi & Richard, 2000; Ishizuka et al., 2014; Marticorena

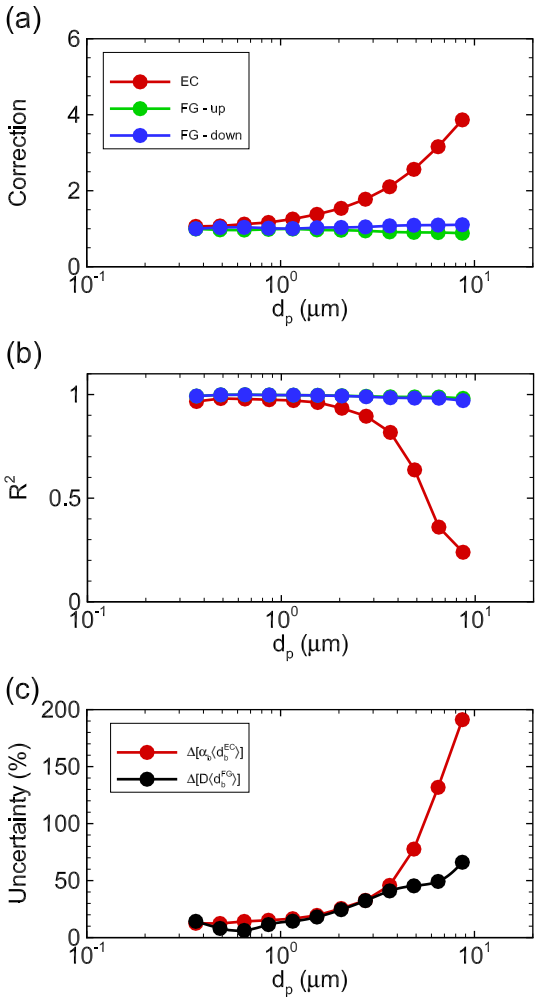

Figure 3. (a) Correction coefficients applied on the EC and FG dust concentrations deduced from the intercomparison experiment. (b) R-squared obtained during the intercomparison experiment from the correlation between the individual FG OPC dust concentrations and between the EC OPC dust concentration and the geometric mean dust concentration of the two FG OPCs (including 750 periods of 1 min). (c) Uncertainties on the difference $D\langle d_b^{FG}\rangle$ between the corrected dust concentrations of the two FG OPCs and on the corrected dust concentration $\alpha_b\langle d_b^{EC}\rangle$ of the EC OPC.

et al., 2006). For comparison purpose, the dust flux was also computed from Equation 7 using the local momentum flux obtained from the sonic anemometer at 3 m AGL instead of assuming a constant momentum flux layer as in Equation 8. This dust flux will be referred hereafter as $F_b^{FG-local}$.

3.4. EC Dust Flux

A third OPC (PALAS, PROMO 2000 equipped with the aerosol sensor WELAS 2300 system) identical to the others was coupled to the 3.0 m AGL sonic anemometer to estimate the correlation between the size-resolved dust concentration fluctuations and the vertical wind velocity fluctuations reduced to the frequency of the OPC (1 Hz) (Figures 1 and 2c). The same calibration as for the two FG OPCs was applied for this OPC.

Since no specific sampling head existed for the OPC to estimate the dust flux by EC, a small sampling head was designed in order to not disturb the measurements of the 3 m AGL anemometer. This head consisted of a 45 cm long and 0.5 cm diameter tube with a drilled cover that allows particles to enter while protecting the inlet from rain (see Figure 2c). Note that the size of the tube was erroneously written as 25 cm long and 1.0 cm in diameter in Dupont et al. (2019). This sampling head was positioned about 20 cm south from the head of the sonic anemometer. This head was made in order (a) to minimize disruption of the air while sampling dust particle within the air and (b) to minimize the time-lag between wind and dust measurements. These constraints were applied at the expense of a truly isokinetic sampling head, the mean flow within the sampling head tube being less than the outside flow during erosion events, 4.2 m s^{-1} versus approximately 8.0 m s^{-1}, respectively.

The 15-min averaged dust flux F_b^{EC} was estimated per size class using Equation 9. Prior to calculating F_b^{EC}, a time-lag correction was applied on the dust fluctuations for each averaging time (15 min), as usually performed in EC when quantities are acquired with different sampling frequencies (e.g., Berg et al., 2015). This time-lag was deduced by maximizing the covariance between the dust concentration and vertical wind velocity fluctuations. Overall, this time-lag remained small, varying between −1 and +2 s, as the dust sensor was very close to the sonic anemometer.

3.5. Quality Control and Correction of the EC Dust Flux

The quality of our EC device (OPC + sampling head + sonic anemometer) was verified on its ability (a) to measure size-resolved dust concentrations and (b) to capture the distributions in frequency of the dust concentration and dust flux, that is, the dust concentration spectrum and dust flux cospectrum, respectively. These controls led us to apply two corrections to the EC dust flux, adding to the time-lag correction (see previous section).

3.5.1. Dust Concentration Correction

During the intercomparison campaign (Section 3.3), the EC OPC was installed at the same height between the two FG OPCs. The intercomparison showed that the EC small sampling head underestimated the dust concentration with increasing particle size and, thus, required a correction.

To correct the EC dust flux obtained during erosion events from an underestimated dust concentration, it is convenient to rewrite the EC dust flux as the product between a transfer velocity $v_{t,b}^{EC}$ and a mean dust concentration C_b:

$$F_b^{EC} = v_{t,b}^{EC} C_b, \quad (12)$$

where $v_{t,b}^{EC}$ corresponds to the ratio between the dust flux $\langle w' d_b^{EC'} \rangle$ and the dust concentration $\langle d_b^{EC} \rangle$, both obtained from the EC device. During dust emissions, $v_{t,b}^{EC}$ informs on the efficiency of the mechanisms, here turbulence and saltation, to transfer dust within the first few meters above the ground, while C_b informs on the magnitude of the source. In the ideal case, $C_b = \langle d_b^{EC} \rangle$. The transfer velocity $v_{t,b}^{EC}$ has the advantage of being independent of the dust concentration magnitude, and thus of not being impacted by a dust concentration underestimation, the ratio between the dust flux and the dust concentration cancels this underestimation, provided the main dust concentration fluctuations are well captured.

By assuming a correct estimation of $v_{t,b}^{EC}$ by the EC device, a first approach to recover the EC dust flux from a dust concentration underestimation, would replace C_b with an independent, well estimated mean dust concentration at the same height as $v_{t,b}^{EC}$. This would correspond to choosing C_b as the geometric mean of the dust concentrations measured by the two FG OPCs, $C_b = \sqrt{\langle d_b^{FG} \rangle_{zdown} \langle d_b^{FG} \rangle_{zup}}$, leading to a dust concentration around the same height as the EC dust flux (3 m AGL). A second approach would involve estimating a correction factor α_b to $\langle d_b^{EC} \rangle$ from the intercomparison between the EC OPC and the two FG OPCs, that is, $C_b = \alpha_b \langle d_b^{EC} \rangle$, and subsequently applying this correction for all erosion events. This last approach was preferred because (a) it leads to less dependency between the EC and FG methods for this comparison exercise, the first approach leading to an EC dust flux constrained every 15-min periods of the erosion events with the mean dust concentration from the FG OPCs and because (b) there was the possibility that the dust concentration of the upper FG OPC may have been impacted during some events by the limited fetch of our plot (see Section 5.2). Nonetheless, the EC dust flux obtained from the first approach will be compared with the FG dust flux, it will be referred hereafter as $F_b^{EC-forced}$ (see Section 4.3).

Hence, the EC dust concentration correction factor α_b was estimated from the linear correlation obtained for each particle size bins between $\langle d_b^{EC} \rangle$ and $\sqrt{\langle d_b^{FG} \rangle_{zdown} \langle d_b^{FG} \rangle_{zup}}$, during the intercomparison campaign. For particle sizes <4 μm diameter, the concentration of the EC OPC correlated well with the average concentration of the two FG OPCs ($R^2 > 0.8$, Figure 3b) allowing a correction factor α_b to be estimated (Figure 3a). For particles with diameter >4 μm, the dust concentration measured by the EC OPC was too low during the intercomparison campaign to attain a good correlation with the concentrations of the two FG OPCs. Nevertheless, a correction factor was estimated for the EC OPC for the same particle size range as the two FG OPCs, that is, up to 9 μm diameter. This correction factor increases with particle size as shown in Figure 3a. The deduced uncertainty of the corrected EC dust concentration (Figure 3c) becomes irrelevant for coarse particles (>4 μm diameter) due to the low concentration of coarse particles during the intercomparison campaign.

To verify the suitability of this correction factor α_b, the average size distributions of the corrected dust number concentration obtained by the EC OPC ($\alpha_b \langle d_b^{EC} \rangle$, from now on we will omit α_b) were compared for each erosion events with the distributions obtained from the geometric mean diameter of the corrected dust concentrations of the two FG OPCs ($\langle d_b^{FG} \rangle_{mean}$) (Figure 4). The dust size distributions appear similar between EC and FG OPCs up to about 5 μm diameter for the March events. For the April events, small differences exist for fine particles, with EC dust concentrations lower than the FG values. Above 5 μm diameter, $\langle d_b^{EC} \rangle$ is most often lower than $\langle d_b^{FG} \rangle_{mean}$ for all events.

3.5.2. High Frequency Dust Flux Correction

The ensemble-averaged 15-min dust spectra are compared in Figure 5 with those of u, w, and θ, for the six erosion events. The velocity and air temperature premultiplied spectra (i.e., multiplied by the frequency) display the familiar shape of atmospheric surface layer spectra in near-neutral conditions (Kaimal et al., 1972), that is, a +1 power law in the energy-containing range of the w-spectra, a u-spectrum peak at lower frequency than that of w-spectra and a flatter peak of the θ-spectra, and a −2/3 power law in the spectrum inertial subrange. The EC dust spectra also exhibit a well-defined energy-containing range with a near +1 power law form, followed by a peak near 0.1 Hz, intermediate between θ- and w-spectrum peak

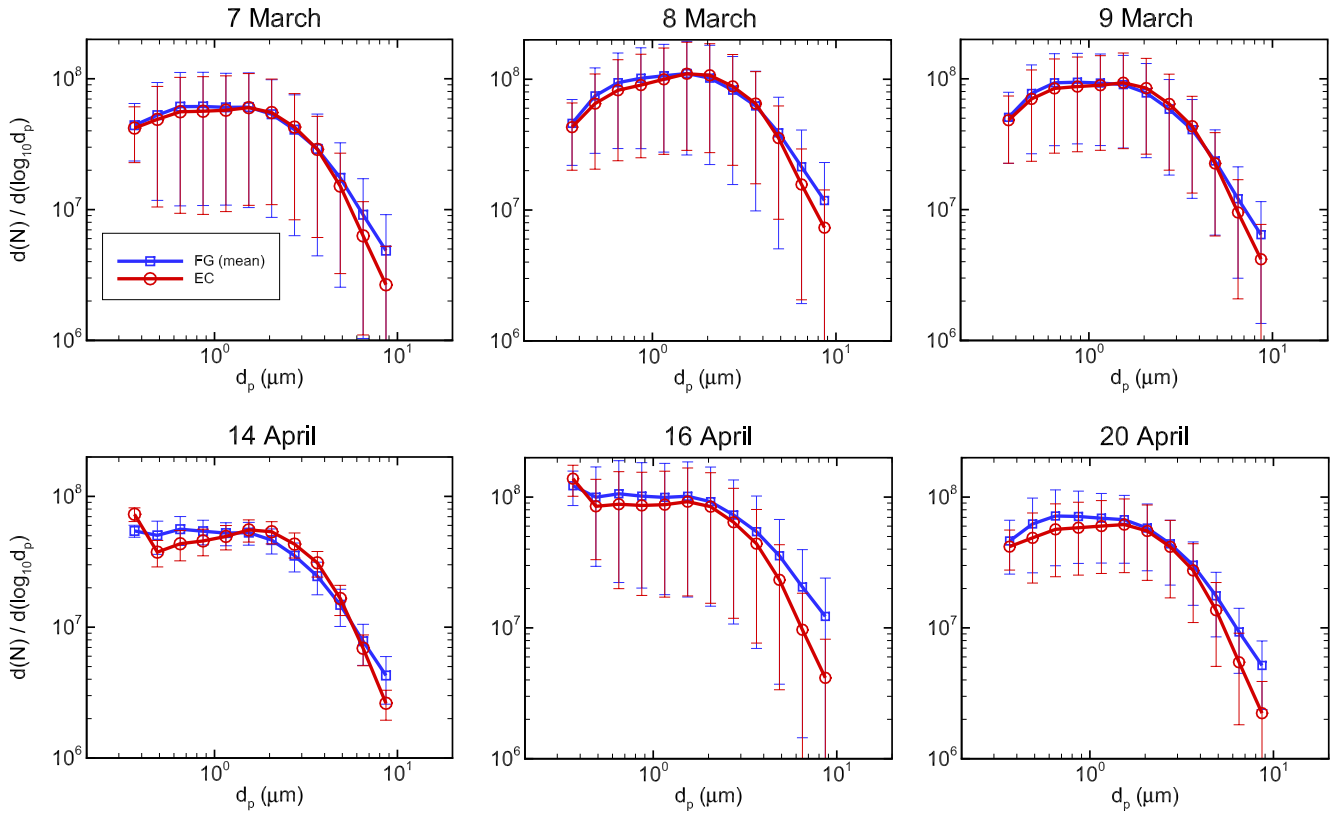

Figure 4. Comparison of the ensemble-averaged size-resolved dust concentrations in number obtained at 3 m height by the EC and FG OPCs using different sampling heads during the six erosion events, after correction of the OPC dust concentrations according to the intercomparison experiment (Figure 3). The FG size-resolved dust concentration is the geometric mean of the dust concentration measured by the two FG OPCs in gradient position. Ensemble-averages were performed over all 15-min periods with well-developed erosion conditions, that is, $u_{*0} \geq 0.25$ ms^{-1}. Error bars correspond to the standard deviations of these ensemble-averages.

positions, before slightly decreasing, depending on the event, with the same slope as the temperature spectra up to the cutoff frequency of the dust sensor.

The ensemble-averaged 15-min *wd*-cospectra are compared in Figure 6 with the *uw*-cospectra for the six erosion events. Figure 6 only presents the *wd*-cospectra of the 2.35 µm diameter bin. Cospectra of other particle sizes are available in Figures S2–S6. Regardless of the particle size, all *wd*-spectra exhibit a parabolic shape, peaking around 0.1 Hz as do the *uw*-cospectra. Past the peak, the *wd*-cospectra decrease on the high frequency side up to the cutoff frequency of the OPC. In the inertial subrange, the slope of the *wd*-cospectra appears slightly steeper than that of the *uw*-cospectra.

It follows from both dust spectra and dust flux cospectra that our EC device is able to capture most of the fluctuations of dust concentration and the main correlations between dust concentration and the vertical velocity fluctuations at the origin of the dust flux. The fact that the shape of the *wd*-cospectra remained very similar between particle sizes, even for the underestimated coarse particles, lends confirmation of the capability of our EC device to measure the concentration fluctuations adequately. We are, therefore, confident that the EC small sampling head had a limited impact on the dust concentrations fluctuations, and only underestimated the dust concentration amplitude with increasing particle size.

As expected, the high frequency part of the dust flux is missed due to the limited 1 Hz sampling frequency of the dust sensor. To quantify the high frequency losses, the *wd*-cospectra are compared in Figure 6 with a standard cospectrum shape accounting for an attenuation on the high frequency side due to the slow-response of the OPC (e.g., Horst, 1997):

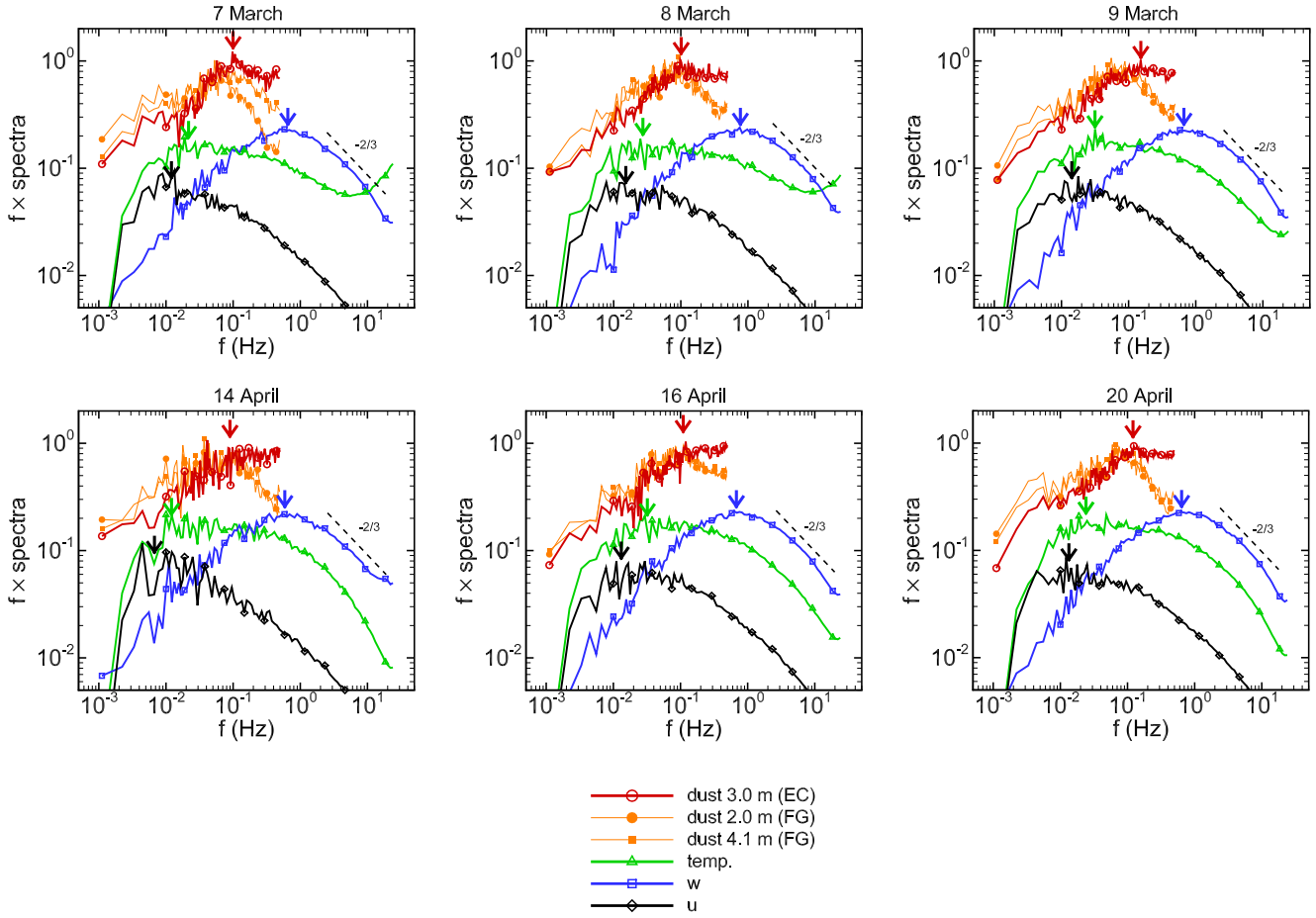

Figure 5. Ensemble-averaged 15-min energy spectra of the longitudinal velocity (u), vertical velocity (w), air temperature (temp.), and total dust number concentration for the six erosion events. The dust spectra include the dust measured at 3.0 m height from the EC OPC equipped with the small sampling head and the dust measured at 2.0 and 4.1 m heights from the FG OPCs equipped with the TSP sampling heads. Dust and longitudinal velocity spectra are shifted upward and downward, respectively, to permit comparison. The arrows indicate the position of the spectrum peaks. Ensemble-averages were performed over all 15-min periods with well-developed erosion conditions, that is, $u_{*0} \geq 0.25$ ms^{-1}.

$$fS_{wd} = \alpha \frac{2}{\pi} \frac{f / f_m}{1 + \left(f / f_m\right)^2} \left(\frac{1}{1 + 2\pi f_m \beta} \right), \tag{13}$$

where S_{wd} is the dust flux cospectrum; f is the frequency; and α, β, and f_m are fitted coefficients that represent, respectively, the true value of the dust flux, the characteristic time constant of the dust sensor response, and the frequency at which fS_{wd} is maximum. The last term between parentheses in Equation 13 represents the attenuation. Compared to this cospectrum shape model, the estimated dust flux appears underestimated at high frequency for some events, between the cospectrum peak and the OPC cutoff frequency (Figure 6). Since the decrease of the d-spectrum between 0.09 and 0.5 Hz was consistent with the θ-spectrum (Figure 5), the steeper slope of the wd-cospectra between 0.3 and 0.5 Hz could be related to a fluctuating time-lag between w and d at scales smaller than the 15-min time period of cospectrum calculation.

The high frequency losses of the dust flux were estimated for each event from the difference between the averaged wd-cospectra and its fitted attenuated parabolic shape (the pink area in Figure 7), and was converted to a correction factor α_{HF} for the EC dust flux. This correction represents on average about +14% of the EC dust flux and shows no clear trend with particle size (Figure 8a), which led us to conclude that α_{HF} is independent of the particle size. Although this correction should increase with wind intensity as dust particles become transported by higher frequency eddies, we only estimated this correction at the scale of

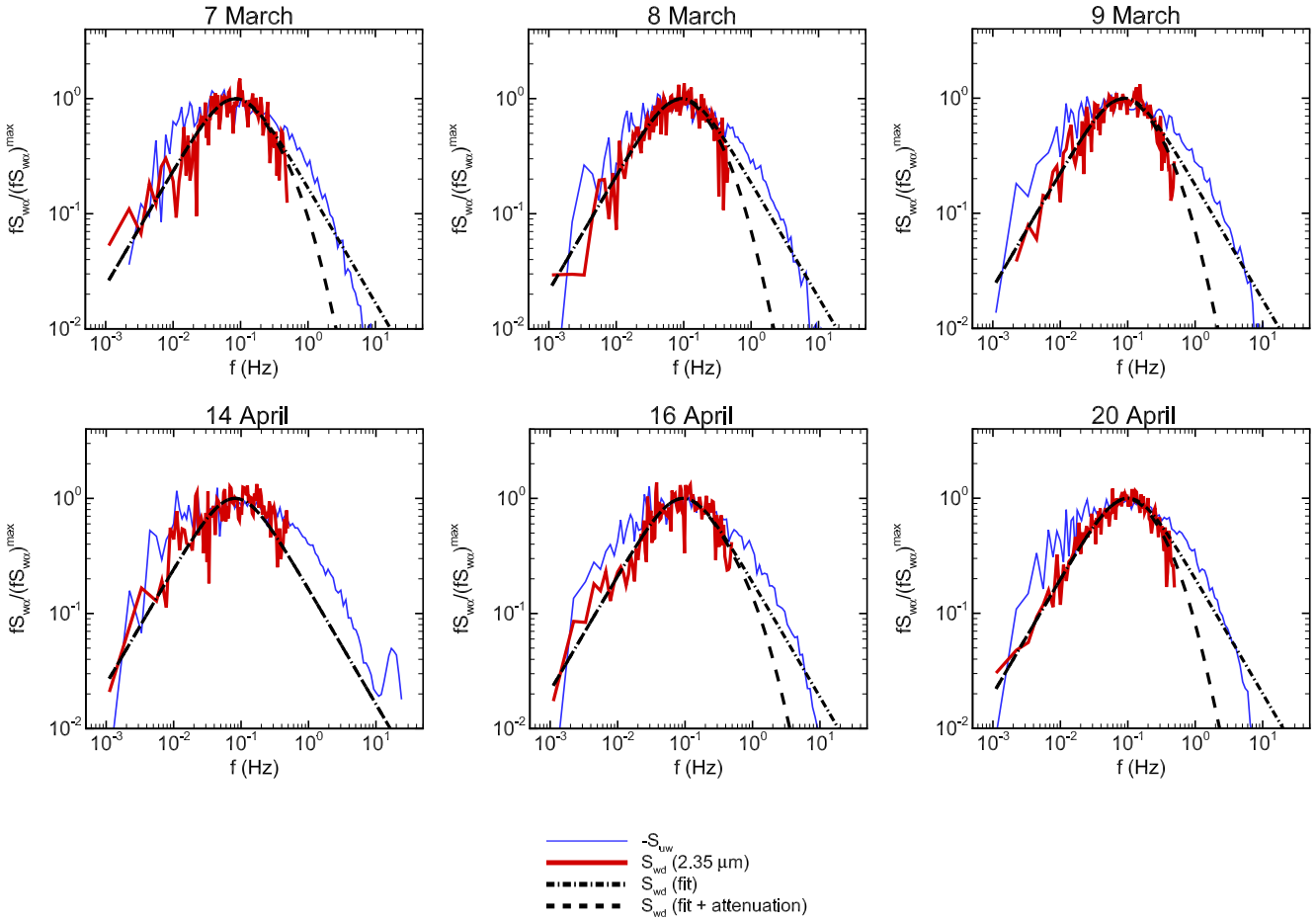

Figure 6. Ensemble-averaged 15-min normalized cospectra of the 2.35 μm-dust fluxes (S_{wd}) compared to that of the momentum flux (S_{uw}), both at 3 m height, for the six erosion events. Fits of the dust flux cospectra with and without high frequency attenuation following Equation 13 are also presented. Cospectra are normalized by their maximum. On the ordinate axis, α is either u or d. Ensemble-averages were performed over all 15-min periods with well-developed erosion conditions, that is, $u_{*0} \geq 0.25$ ms^{-1}. Equivalent figures for the other particle size bins are available in supplementary material.

the erosion events because (a) the wind intensity did not vary much during the events to induce a significant variation in this correction (see u_{*0} in Table 1) and because (b) the dust and momentum flux cospectra at 15-min time intervals were still too perturbed to evaluate accurately the high frequency loss of the dust flux by comparison to the momentum flux.

Finally, it is worth noting (a) the damping at frequencies higher than 0.1 Hz of the dust concentration fluctuations measured by the two FG OPCs using the TSP sampling heads when comparing the FG dust spectra with the θ spectra (Figure 5) and (b) the lower frequency of EC dust spectrum peaks compared to the w spectrum peaks. The first observation confirms the unsuitability of the TSP sampling heads for performing EC. The second observation means that the characteristic scales of the vertically transporting eddies are smaller than the scales over which the dust gradient may change appreciably. This supports the conditions of application of the FG method although the difference in frequency between w- and d-spectrum peaks is smaller than that between w- and u- or θ-spectrum peaks.

4. Results

4.1. Dust Flux

The average magnitude of the total dust flux per event as obtained from the FG method are consistent with the usual values reported in the literature using the same method. In number, $F_{n,tot}^{FG}$ (Equation 10) varies from 1.0 to 2.5 × 10^7 #m^{-2} s^{-1}, with maximum values up to 10.0 × 10^7 #m^{-2} s^{-1} (Table 1). In mass,

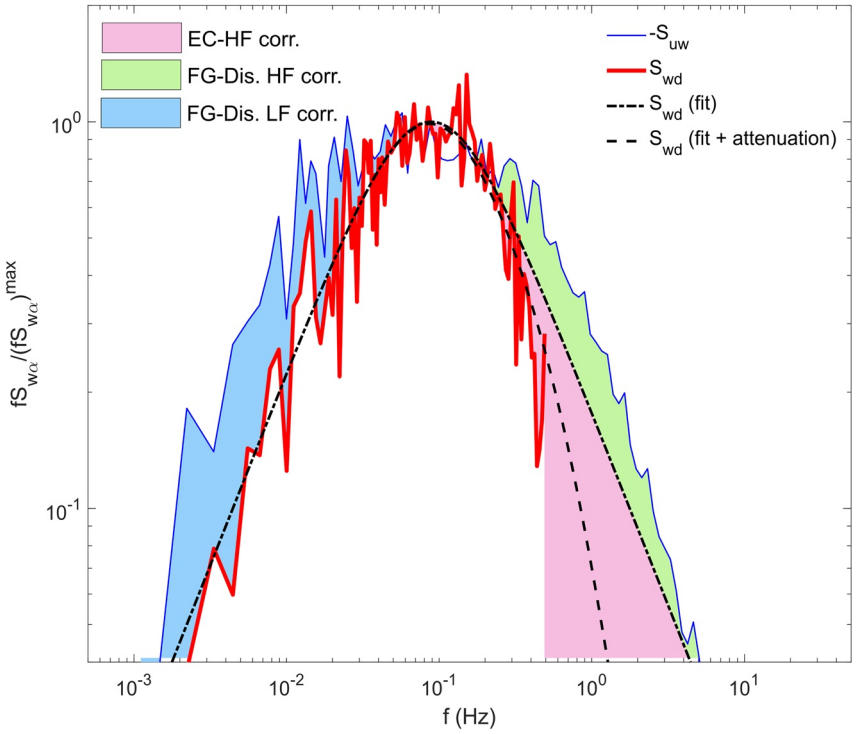

Figure 7. Illustration for the 9 March event of the corrections estimated from the cospectra of the 2.35 µm-dust (S_{wd}) and momentum fluxes (S_{uw}) as presented in Figure 6. EC-HF correction refers to high frequency losses of the EC dust flux (Section 3.5), FG-Dis. LF and FG-Dis. HF refer to the low and high frequency corrections, respectively, of the FG flux due to the dissimilarity in turbulent transport between momentum and dust (Section 5.3).

$F_{m,tot}^{FG}$ (Equation 11) varies from about 190 to 830 µg m^{-2} s^{-1}, with maximum values up to 4,270 µg m^{-2} s^{-1} (Table 1). The same order of values were reported by Sow et al. (2009) and Ishizuka et al. (2014), around 100–2,000 µg m^{-2} s^{-1}.

In Figure 9, the time variations of $F_{n,b}^{EC}$ and $F_{n,b}^{FG}$ are compared during the six erosion events and for three particle size ranges: 0.37–0.87 µm (fine dust particles), 1.15–3.65 µm (medium size), and 4.87–8.66 µm (coarse). As expected, without erosion, that is, for friction velocities lower than the erosion threshold value (0.22 m s^{-1}), the EC method predicts a zero dust flux and the FG method presents no values as there is no significant difference between dust concentration at the two levels. During the periods of erosion, both methods predict remarkably well the same dynamics with time of the dust flux for all particle size ranges. For fine and medium size particles, the magnitudes of the fluxes are in good agreement between methods during the March events, with a difference per event <14% of the EC dust flux and a RMSE (Root Mean Square Error) per event <44% (Table 2). During April events, $F_{n,b}^{EC}$ is lower than $F_{n,b}^{FG}$ for fine particles (also for medium-size particles for the 16 April event), with a difference ranging between −37% and −54%, and a RMSE between 49% and 69%. For coarse particles, $F_{n,b}^{EC}$ is always significantly lower than $F_{n,b}^{FG}$ for all events with values ranging from −49% to −158%, and a RMSE varying from 71% to 272%. This difference between fluxes is discontinuous with some periods of good agreement such as the end of the 8 March event or most of the 9 March event.

As expected, without correcting the EC dust concentration (Section 3.5.1), the EC dust flux remains close to the EC dust flux with correction for fine particles (Figure S7). This correction only becomes significant for larger particles. For medium-size particles, this correction allows the EC dust flux to better match the FG dust flux, while for coarse particles this correction appears insufficient for the EC flux to reach the FG values.

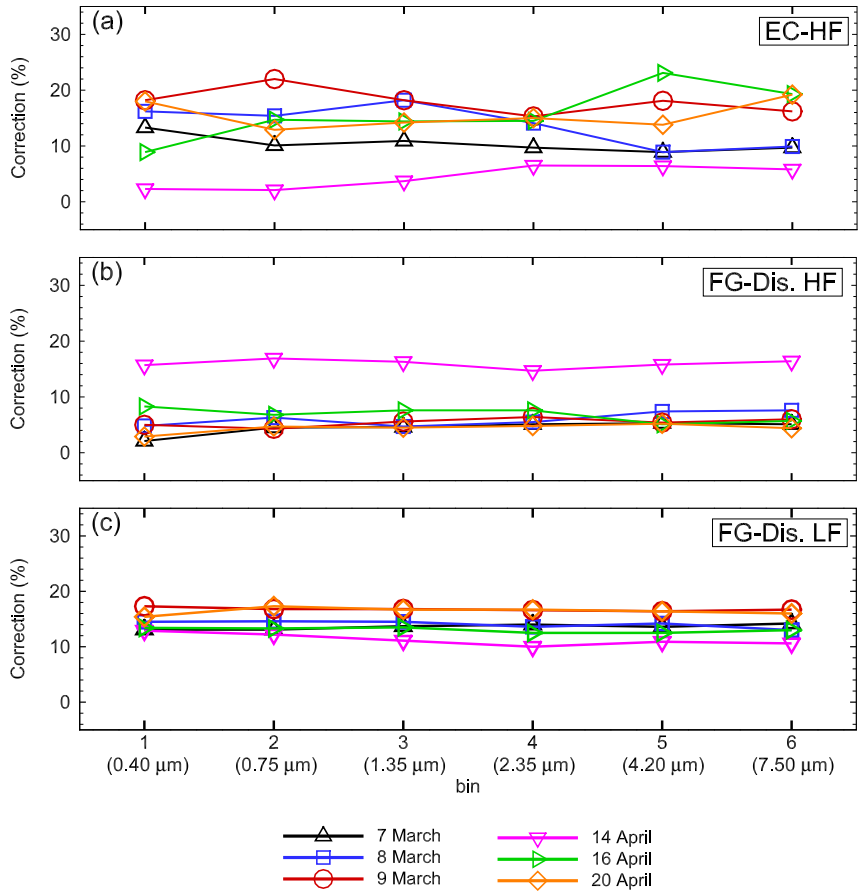

Figure 8. Variation of the corrections applied to the EC and FG dust flux with particle size according to the erosion event. Corrections are expressed in percentage of the uncorrected flux. (a) EC-HF correction refers to high frequency losses of the EC dust flux (Section 3.5). (b and c) FG-Dis. LF and FG-Dis. HF refers to the low and high frequency corrections, respectively, of the FG flux due to the dissimilarity in turbulent transport between momentum and dust (Section 5.3).

The average size distributions of the EC and FG dust fluxes (in number) exhibit two modes, one peaking near 0.65 µm and one near 1.50 µm (Figure 10), as already evidenced by Khalfallah et al. (2020) for the FG dust fluxes. Considering the particle size distribution of the plot soil, the submicron mode may correspond to individual clay particles present in the soil, and the supermicron one to aggregates of clay particles. The contribution of these two modes in the dust flux differs slightly between the EC and FG fluxes, depending on the event. Both methods agree on the dominance of the coarser mode during the 7, 8 March and 20 April events. For the other events, the EC method predicts a larger contribution of the coarser mode while the FG method predicts either a similar contribution of both modes or a slightly larger contribution of the finer mode. Overall, the average size distributions of both fluxes remain quite close, within the standard deviations of these ensemble-averages.

4.2. Uncertainties on the FG and EC Dust Fluxes

Although the uncertainties on the FG and EC dust fluxes cannot explain the mean difference observed between FG and EC fluxes, they quantify the random errors around the mean dust flux values and thus indicate the level of confidence on the flux values. The uncertainties of the FG and EC dust fluxes due to measurement errors have been estimated following the procedure described in Appendix A. For the FG dust flux, the uncertainty is mainly related to the dust concentration, and for the EC dust flux to both the sampling error and the corrected dust concentration. The global uncertainties obtained for each erosion event are presented according to the particle size in Figure 11 and for the three particle size ranges in Table S1.

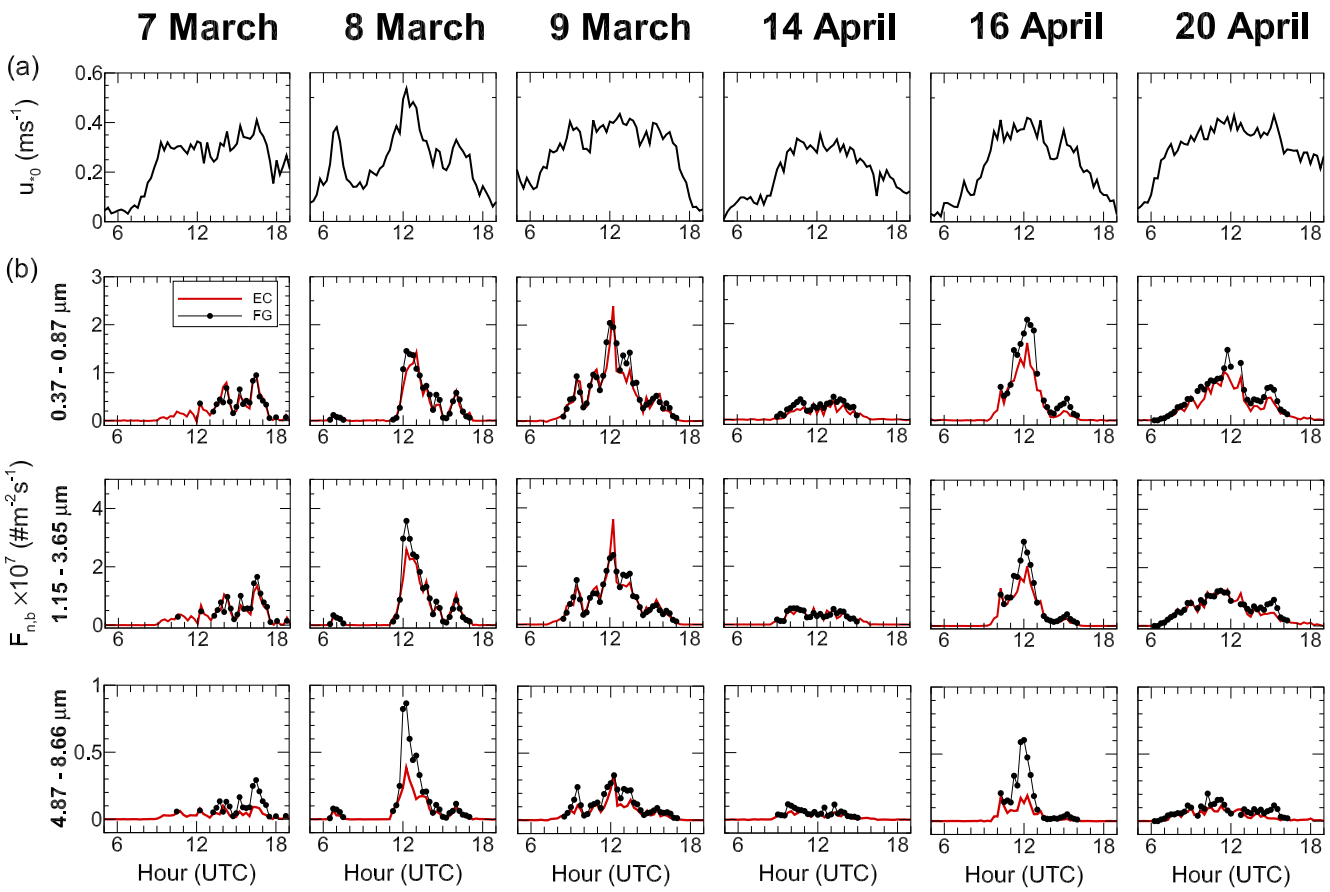

Figure 9. Comparison between the EC and FG dust fluxes as a function of time during the six wind erosion events. (a) Time variation of the surface friction velocity (u_{*0}) deduced from the sonic anemometers according to Dupont et al. (2018). (b) Comparison between the EC and FG dust fluxes in number and for three particle size ranges: 0.37–0.87 µm, 1.15–3.65 µm, and 4.87–8.66 µm.

Overall, the uncertainty on the FG dust flux is lower than on the EC dust flux, especially for coarse particles (Table S1). The uncertainties range for fine to medium-size particles around 9% and 16% for the FG and EC dust fluxes, respectively, and around 31% and 71% for coarse particles. With particle size, the uncertainty on the FG dust flux is lower for particles around 0.55 µm (±10%), and increases with particle size. The uncertainty on the EC dust flux is also lower for particles around 0.4–1.5 µm (±28%), and then increases exponentially with particle size. This uncertainty is dominated for fine particles by the sampling error uncertainty, with values typical of EC fluxes, and for coarse particles by the uncertainty on the corrected dust concentration. The uncertainties of both FG and EC dust fluxes do not vary much with events because the uncertainties on the dust concentration, or corrected dust concentration, were estimated relative to the intensity of the concentration.

Table 2
Difference and Root Mean Square Error (RMSE) Between EC and FG Dust Fluxes in Number, for Three Particle Size Ranges: 0.37–0.87, 1.15–3.65, and 4.87–8.66 µm

	EC versus FG					
	0.37–0.87 µm		1.15–3.65 µm		4.87–8.66 µm	
Events	Diff.	RMSE	Diff.	RMSE	Diff.	RMSE
7 March	2%	23%	−11%	36%	−123%	170%
8 March	−11%	36%	−14%	44%	−91%	177%
9 March	−12%	34%	1%	28%	−49%	71%
14 April	−54%	63%	−9%	29%	−56%	84%
16 April	−47%	69%	−32%	59%	−158%	272%
20 April	−37%	49%	−12%	28%	−61%	89%

Note. Both quantities are expressed in percentage of the EC dust flux.

For fine and medium-sized particles, the lower uncertainty of the FG dust flux compared with the EC-derived flux, is mainly explained by the dependence of the FG method on only first order moments (mean velocity, mean dust concentration, mean temperature) while the EC method depends on a second order moment (correlation between wind velocity and dust concentration).

For both methods, the increase of the dust flux uncertainty with particle size is not related to the method itself but to the low concentration of

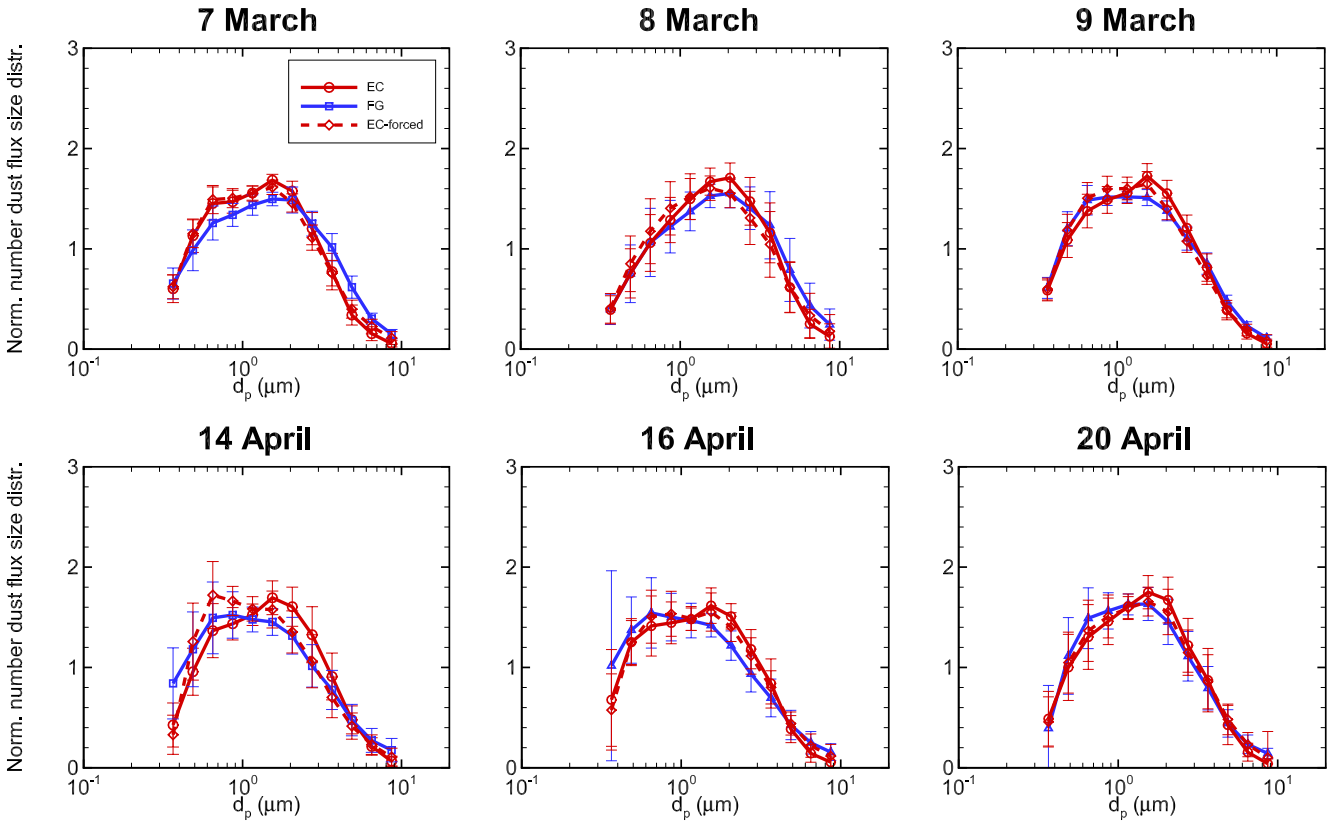

Figure 10. Comparison between the ensemble-averaged size distributions of the EC and FG dust fluxes in number for each erosion event. The size distribution of the EC-forced dust flux is also presented. In EC-forced, the EC dust flux is constrained with the geometric mean concentration of the two FG OPCs (Section 3.5). Ensemble-averages were performed over all 15-min periods with well-developed erosion conditions, that is, $u_{*0} \geq 0.25$ ms^{-1}. Error bars correspond to the standard deviations of these ensemble-averages.

these particles during the intercomparison campaign. This did not allow us to estimate accurately the mean dust concentration of the coarsest particles and so the concentration correction of the EC device.

4.3. EC Dust Concentration Correction

To investigate the role played by the EC dust concentration correction on the difference between EC and FG dust fluxes, we further constrained the EC dust concentration correction toward the

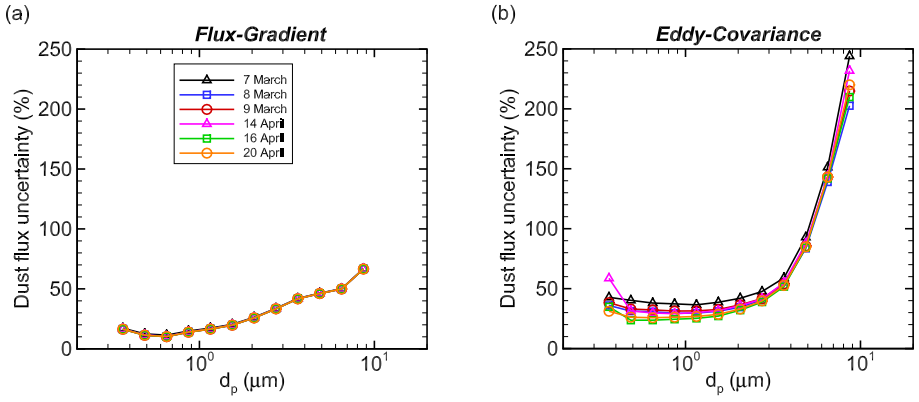

Figure 11. Total uncertainties of the EC and FG dust fluxes according to the particle size for each erosion events (see Appendix A).

Table 3
Same as Table 2 but Between EC-Forced and FG Dust Fluxes

	EC-forced versus FG					
	0.37–0.87 μm		1.15–3.65 μm		4.87–8.66 μm	
Events	Diff.	RMSE	Diff.	RMSE	Diff.	RMSE
7 March	10%	23%	−10%	27%	−62%	96%
8 March	1%	26%	−16%	41%	−57%	113%
9 March	−3%	28%	−3%	30%	−28%	56%
14 April	−27%	37%	−19%	31%	−53%	73%
16 April	−24%	40%	−17%	40%	−43%	98%
20 April	−10%	28%	−3%	23%	−11%	55%

Note. Here, EC-forced refers to the EC dust flux constrained with the geometric mean dust concentration of the two FG OPCs (Section 3.5).

concentration measured by the FG OPCs. Instead of correcting the EC dust concentration with a constant correction factor ($C_b = \alpha_b \langle d_b^{EC} \rangle$, see Section 3.5.1), we replace here C_b by the geometric 15-min mean dust concentration of the two FG OPCs. This new EC dust flux is referred hereafter as $F_b^{EC-forced}$. With this forcing, the difference between the EC and FG dust fluxes is reduced for coarse particles but still remains significant, ranging from −11% to −62% (55%–113% in RMSE) (Table 3). For fine and medium-size particles, the improvement is small, depending on the events. The size distribution of the EC dust flux remains similar, with only a slightly better agreement for the 9 March and 14 April events (Figure 10).

In conclusion, even after constraining the EC dust concentration with the FG dust concentration, differences persist between EC and FG dust fluxes, especially for coarse particles. This suggests that the difference of sampling heads between the OPCs used by both methods does not explain all the differences in flux between both methods, in particular for coarse particles.

4.4. Dust Transfer Velocity

Another way to evaluate the EC and FG methods is to compare their predicted dust transfer velocities v_t^{EC} and v_t^{FG}, respectively. Compared to the dust flux, v_t does not depend on the dust concentration correction, the ratio between the dust flux and the dust concentration canceling this correction (see Section 3.5.1). Here, v_t was estimated for the three particle size ranges (0.37–0.87, 1.15–3.65, and 4.87–8.66 μm) using for EC the concentration measured by the EC OPC at 3 m AGL and for FG the geometric mean dust concentration of the two FG OPCs.

Figure 12 compares the time variation of v_t^{EC} and v_t^{FG} for fine and coarse particles, for the six events. Overall, v_t of both methods exhibits the same order of magnitude for all erosion events and particle size ranges. This result is remarkable knowing the significant differences of intensities of the dust concentrations and fluxes

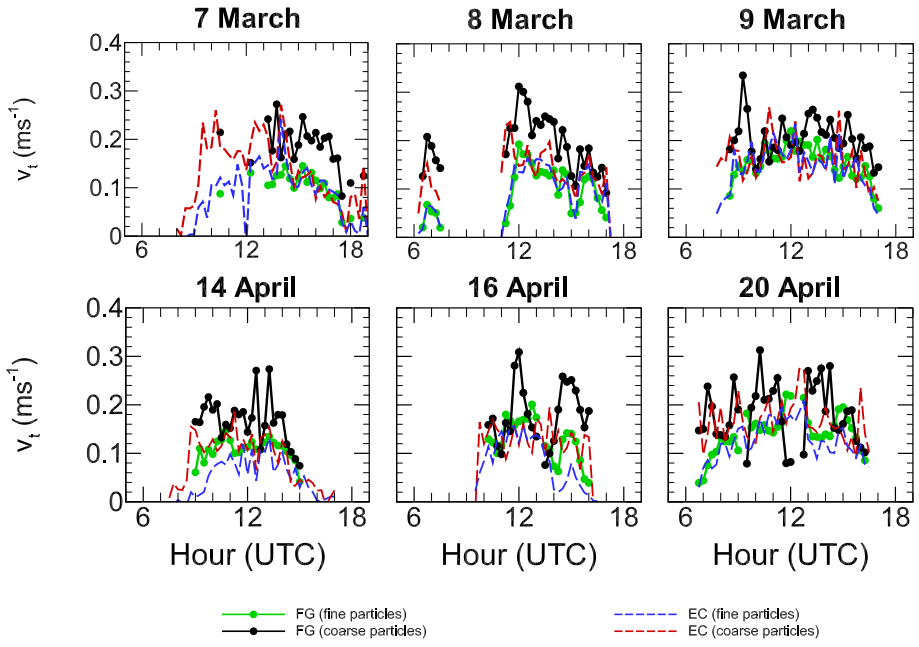

Figure 12. Time variation of the transfer velocities v_t obtained from the EC and FG dust fluxes for the fine and coarse particle size ranges (0.37–0.87 μm and 4.87–8.66 μm, respectively), for the six erosion events.

between events and particle sizes. Despite the large uncertainty on the EC dust concentration correction and the difference in flux amplitude between EC and FG, v_t^{EC} of coarse particles remains consistent with the velocity values of fine particles and close to the FG values. This demonstrates the robustness of EC in still capturing the mechanisms of dust transfer (correlations between w and d_b) despite the underestimation of coarse dust concentrations.

Both methods agree well especially for fine particles, with some exceptions at the beginning and end of the 14 and 16 April events, respectively. For coarse particles, the differences are more important. FG often predicts a larger v_t than EC, but also v_t^{FG} appears more scattered, which is surprising since FG depends only on first order moments while EC depends on a second order moment.

Regardless of the amplitude differences between v_t^{EC} and v_t^{FG}, the distinction of v_t between particle sizes as predicted by EC and FG changes with time. Three different periods emerge from Figure 12. First, the periods where both methods predict a lower v_t for fine particles. These periods occur preferentially during the first hours (up to 7 h) of erosion events, as well as at the end of the April 16, event. It is believed that this lower v_t for fine particles results from their background concentration present before or at the end of the erosion events, while the background of coarse particles is negligible (see Figure S8). This background impacts the concentration used to evaluate v_t of fine particles when this background is of the same magnitude as the fine dust concentration during the event. As the event intensifies, this background becomes negligible, bringing the v_t of fine particles closer to that of coarse particles. Second, the periods where both methods predict a similar v_t between fine and coarse particles, which happens rarely (10:00–12:00 on 9 March, 14:00–15:00 on 14 April, 10:30–11:30 on 16 April). Third, the periods where EC predicts a similar v_t between fine and coarse particles while FG predicts a larger v_t for coarse particles. This is in particular visible during the following periods: 15:00–18:00 UTC of 7 March, 12:00–14:30 UTC of 8 March, 09:30–10:00 and 12:30–13:30 UTC of 9 March, and 11:30–12:30 UTC of 16 April, where v_t^{FG} reaches some of its largest values, in particular for the 8 March and 16 April. Interestingly, during these periods, the difference between the EC and FG dust fluxes of coarse particles is the largest (see Figure 9). This means that the periods of discrepancy between v_t^{EC} and v_t^{FG} represent an additional reason to the EC dust concentration correction underestimation, for explaining the difference between the EC and FG dust fluxes of coarse particles. This is confirmed by the similar differences in percentage between v_t^{EC} and v_t^{FG} and between $F_{n,b}^{EC-forced}$ and $F_{n,b}^{FG}$ at the scale of the erosion events (Tables S2 and 3). Reasons for this difference between v_t^{EC} and v_t^{FG} are discussed in the next section.

5. Discussion

The comparison between the EC and FG size-resolved dust fluxes showed overall a good agreement for fine and medium-size particles with some exceptions for April events (Table 2). For coarse particles, a systematic difference was observed for all events, with EC dust fluxes lower than FG ones. Part of this difference can be explained by the underestimation of the EC dust concentration correction related to the EC sampling head. However, a significant difference persists after constraining the EC dust flux with the FG dust concentration. Interestingly, the difference between EC and FG dust fluxes was not uniform among the erosion events and seems correlated with periods where the particle transfer velocity behaves differently with particle size between EC and FG methods: v_t^{EC} remaining similar between fine and coarse particles while v_t^{FG} was larger for coarse particles.

As described in Section 2, the EC method is a direct method leading to a local estimate of the flux at the height where both the vertical wind velocity and the dust concentration fluctuations are measured. On the other hand, the FG method estimates the flux in a fluid layer between the two FG dust concentration sensors, and considering several hypotheses. In particular, (a) dust turbulent transport is assumed local across the bulk gradient between the two dust levels, without large-scale dust advection and turbulent transports, (b) the two measurement positions are considered located within the same boundary layer established with the underneath surface (Figure 1), and (c) dust particles are presumed similarly transported by turbulence as momentum. These first two hypotheses correspond to constant momentum and dust flux layers across the fluid layer between the two FG dust sensors, and the third one is known as the similarity assumption.

Not meeting the restrictions of these three hypotheses could become critical in presence of an erodible plot with a limited fetch and for intermittent erosion events. The first hypothesis means that if the upper level

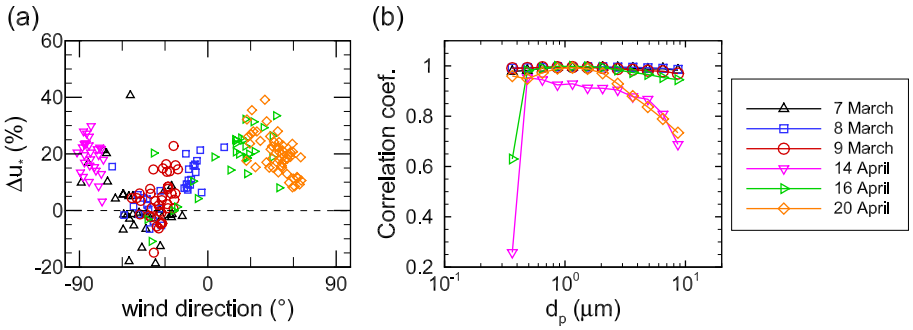

Figure 13. (a) Difference Δu_* in percentage between u_* at 4.1 and 1.9 m height relative to u_* at 1.9 m as a function of the mean wind direction, for the 15-min periods of each erosion event. (b) Correlation coefficients between the time-varying FG upper and lower 15-min averaged dust concentrations according to the particle diameter size for each events.

is in the discontinuity region of the internal boundary layer developing from the upwind edge of the dust source plot (Figure 1), then non-local turbulent transport or horizontal advection of dust from outside the internal layer might become significant, breaking the local connection between the dust flux and the dust concentration gradient through the local eddy diffusivity (Equation 2). The second hypothesis assumes that the two levels should be located within the equilibrium sublayer of the internal boundary layer. If the upper level is above or in the discontinuity region then this upper level might be decoupled from the lower level, and the FG dust flux might be overestimated (underestimated) due to the lower (higher) upper dust concentration coming from the less (more) erodible upwind plots. The third hypothesis is usually justified in three-dimensional homogeneous turbulence for dust particles smaller than 20 μm, the particle trajectory crossing effect being negligible (Shao, 2008). However, close to the surface, Dupont et al. (2019) observed a difference in turbulent transport between dust and momentum during moderate wind erosion events due to the intermittency of dust emission compared to the more continuous absorption of momentum by the surface.

The verification of these hypotheses and their consequences on the comparison between the EC and FG dust fluxes are discussed in the next sub-sections.

5.1. Constant Momentum-Flux Layer

Figure 13a presents for the six erosion events the percentage of u_* variation across the fluid layer considered by the FG method (between 2.0 and 4.1 m height), relative to u_* at 1.9 m, as a function of wind direction. A constant momentum flux layer appears well verified for north-westerly winds, corresponding to most of the March events and the beginning of the 16 April event. For other wind directions, that is, mostly April events, u_* is larger at 4.1 m height. This weakening of the constant momentum flux layer is probably related to the short fetch of the plot and the presence of rougher surfaces upstream from our plot. It is therefore possible that for winds other than north-westerly, the top of the profile was contaminated by turbulence established with the rougher upwind surface outside the plot, although the mean velocity profile was well approximated by a logarithmic function (Dupont et al., 2018).

To evaluate the impact of this weak constant flux layer on the calculation of the FG dust flux, we compared the time variation of $F_{n,b}^{FG}$, where the local momentum flux at the height of the dust flux is taken to be equal to the momentum flux at the surface (Equation 8), with $F_{n,b}^{FG-local}$, where the dust eddy diffusivity is estimated from the local u_* instead of the surface u_{*0} (Equation 7). Knowing that the momentum flux is not perfectly constant with height (Figure 13a) and that the EC dust flux represents a local flux, we expected $F_{n,b}^{FG-local}$ to be closer to $F_{n,b}^{EC}$ than $F_{n,b}^{FG}$. Surprisingly, the opposite was observed (Figure S9). The difference and RMSE between EC and FG-local dust fluxes are enhanced (Table 4 compared to Table 2). This is observed for all particle sizes and all events, with larger differences between FG and FG-local for the 20 April event, the event with the weakest constant momentum flux layer.

Table 4
Same as Table 2 but Between EC and FG-Local Dust Fluxes

	EC versus FG-local					
	0.37–0.87 μm		1.15–3.65 μm		4.87–8.66 μm	
Events	Diff.	RMSE	Diff.	RMSE	Diff.	RMSE
7 March	−22%	36%	−36%	54%	−172%	214%
8 March	−35%	63%	−37%	69%	−127%	226%
9 March	−40%	62%	−22%	35%	−83%	107%
14 April	−147%	164%	−75%	91%	−152%	189%
16 April	−82%	112%	−62%	93%	−215%	352%
20 April	−102%	123%	−67%	85%	−142%	178%

Note. In FG-local dust flux, the momentum eddy diffusivity is estimated locally, without assuming a constant momentum flux layer (Equation 7).

We suspect that $F_{n,b}^{FG}$ is better representative of the surface dust flux than $F_{n,b}^{FG-local}$ because $F_{n,b}^{FG}$ is closer to $F_{n,b}^{EC}$ for fine dust particles, a particle size range over which the EC dust flux can be trusted due to the negligible impact of the EC OPC sampling head on the dust concentration. The better match between the FG and EC dust fluxes than between the FG-local and EC dust fluxes means that the dust exchange process between neighboring turbulent eddies at 3 m AGL, as considered by the FG relationship (K-theory) and here by the FG-local flux, is not perfectly verified during our experiment. At 3 m AGL, downward eddies bringing higher turbulence from above the internal boundary layer might occur, explaining the slight increase of the momentum flux and the higher eddy diffusivity than at the surface. This higher eddy diffusivity leads to an over-prediction of the dust flux by the FG-local method. Fortunately, the FG relationship seems to be recovered from the weak constant momentum flux layer when considering the turbulence properties close to the surface where dust emission occurs.

5.2. Constant Dust Flux Layer

Conversely to the momentum flux layer, our measurements did not allow us to check directly for the existence of a constant dust flux layer between 2.0 and 4.1 m. It is possible that the relative difference of dust emission between our plot and the surrounding surfaces was more important than that of absorbed momentum between the same surfaces. Consequently, a larger fetch might be required to reach a constant flux layer for dust than for momentum.

The correlation between the temporal dynamics of the 15-min mean dust concentrations measured by the two FG dust sensors at 2.0 and 4.1 m height provides a means to verify that both FG sensors were sensitive to the same temporal variation of the source, but it does not demonstrate that they were located in the same dust internal boundary layer developing from the upwind edge of the erodible plot. Only a poor correlation would prove that both levels were not in the same boundary layer. For March events, the time-varying FG upper and lower 15-min averaged dust concentrations appear well correlated (>0.95, Figure 13b), this correlation is weaker (lower than 0.9) for fine (<0.7 μm) and coarse (>3.0 μm) particles for the 14 and 20 April events. For fine particles, this may be explained by the presence of particles that are not mineral dust. For coarse particles, this may suggest that the upper sensor might be influenced by the flow above or upstream from the dust internal boundary layer developing from the upwind plot edge. This result is consistent with the weaker momentum flux layer observed for these erosion events.

Although Figure 13b does not represent a demonstration of the absence or presence of a constant dust flux layer, we cannot reject the possibility that the difference between EC and FG dust fluxes for coarse particles is also related to the weakening of the dust constant dust flux layer at 4.1 m high. The fact that the largest discrepancy between the EC and FG dust fluxes for coarse particles occurs when the FG dust transfer velocity of coarse particles reaches larger values than the fine particle values, while the EC transfer velocities remain similar between particle sizes, provides an additional reason to suspect that the constant dust flux layer for coarse particles at the level of the upper FG dust sensor was weakening.

5.3. Dissimilarity in Turbulent Transport Between Dust and Momentum

One evidence of the dissimilarity in turbulent transport between dust and momentum is the difference in the distributions of the normalized dust and momentum fluxes with eddy frequency (cospectra), as represented on the low frequency side by the blue area in Figure 7 and to a lesser extent on the high frequency side by the green area. These differences reflect the increased efficiency of large and small eddies at transporting momentum than dust. The lower efficiency of large eddies at transporting dust was attributed by Dupont et al. (2019) to the intermittency of dust emission compared to the more continuous absorption of momentum by the surface. This was observed for all particle sizes. Hence, assuming similarity in turbulent transport between momentum and dust should lead to an overestimation of the dust flux.

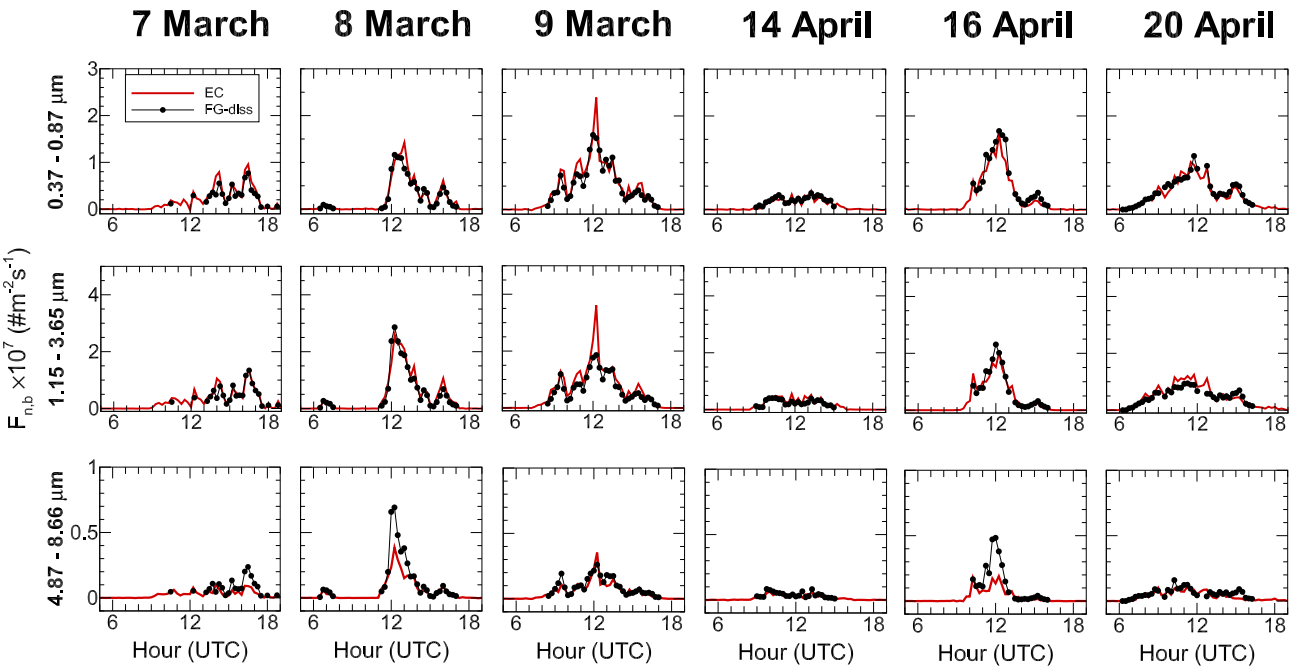

Figure 14. Same as Figure 9b but between EC and FG-diss, where the FG-diss dust flux includes corrections due to the dissimilarity between momentum and dust turbulent transports.

We corrected the FG dust flux for dissimilarity between momentum and dust transports by removing the extra fraction of the normalized momentum flux on the low and high frequency sides compared to the normalized EC dust flux (blue and green areas). This correction represents about 0% to −16% of the FG flux for the high frequency side and −11% to −17% for the low frequency side (Figures 8b and 8c). These corrections were estimated independently of the particle size, as no clear trend of these corrections was observed with particle size.

Overall, the application of this correction on the FG dust flux (referred to as FG-diss) brings it closer to the EC flux (Figure 14) for the April events and for coarse particles of all events, reducing the difference and RMSE between both fluxes (Table 5 vs. Table 2). The match between EC and FG-diss dust fluxes for fine and medium-size particles is less improved for March events, the EC dust flux being slightly larger than the FG-diss flux. We cannot exclude that a part of the dissimilarity observed between dust and momentum turbulent transport could be also explained by the limited depth of the dust internal boundary layer due to the small fetch of our plot for some of the events, as demonstrated numerically by Fernandes et al. (2020).

Table 5
Same as Table 2 but Between EC and FG-Diss Dust Fluxes

	EC versus FG-diss					
	0.37–0.87 µm		1.15–3.65 µm		4.87–8.66 µm	
Events	Diff.	RMSE	Diff.	RMSE	Diff.	RMSE
7 March	20%	33%	10%	31%	−80%	123%
8 March	11%	32%	9%	27%	−53%	119%
9 March	12%	32%	23%	40%	−16%	45%
14 April	−12%	32%	21%	34%	−14%	48%
16 April	−17%	36%	−5%	32%	−107%	195%
20 April	−7%	24%	13%	31%	−25%	59%

Note. FG-diss refers to the FG dust flux after applying corrections for the dissimilarity in turbulent transport between momentum and dust (Section 5.3).

6. Conclusions

For the first time the size-resolved dust flux has been estimated using both the FG and the EC methods for several wind erosion events recorded during the WIND-O-V's 2017 field experiment. Overall, good agreement between the dust fluxes estimated by both methods was obtained for fine (0.37–0.87 µm) and medium-size (1.15–3.65 µm) dust particles, confirming the applicability of the EC method for this particle size range. Both methods were able to reproduce the same temporal dynamics of the dust fluxes, the same two particle diameter modes (0.65 and 1.5 µm), and close dust flux amplitudes with the average difference <23% and RMSE <40% for the daily March events.

For coarse particles (4.87–8.66 μm), the EC fluxes were always smaller than the FG fluxes with on average over erosion events a difference of −88% and a RMSE of 139%, but with some periods of agreement. Part of the difference is related to the underestimation of the dust concentration by the EC OPC due to the small sampling head required to not impact the sonic anemometer measurements. This EC dust concentration correction could not be estimated accurately for coarse particles. A full constraint of the EC dust concentration from the FG dust concentration reduced the difference between EC and FG fluxes by approximately half, suggesting that the EC dust concentration correction could not solely explain the difference between the methods. Interestingly, the transfer velocity of coarse particles estimated from the EC method was of the same order as the fine particles, suggesting that the fundamentals of the EC technique correlating the vertical velocity component and the dust concentration fluctuations was also valid for the coarsest particles, even though the amplitude of the dust concentration of coarse particles was underestimated by the EC sampling head. This means that the EC technique can be used to estimate the flux of coarse particles (<10 μm) as the product of the particle transfer velocity deduced by the EC device and a mean dust concentration measured at the same height from a low frequency OPC equipped with an appropriate sampling head.

The periods with the largest differences between EC and FG fluxes of coarse particles correspond to periods where the FG transfer velocities are the highest for coarse particles, with values larger than for fine particles, while the EC transfer velocities remain similar between coarse and fine particles. It is, therefore, possible that the difference between the EC and FG fluxes of coarse particle was also related to the conditions of applicability of the FG method.

It appears that the dust eddy diffusivity ($K_{d,b}$) used in the FG method was challenged by the short fetch length of our experimental plot and the intermittency of moderate erosion events. First, the hypothesis of local dust eddy diffusivity of the dust FG relationship was not verified due to the short fetch of our plot. Fortunately, the use in $K_{d,b}$ of turbulence characteristics (friction velocity) at the surface, where dust emission occurs, instead of local turbulent characteristics (3 m high, here), allowed us to recover the applicability of the FG relationship in the context of a weak constant momentum flux layer. This showed (a) the sensitivity of the FG dust flux to the turbulence scale used in $K_{d,b}$ in case of a weak constant momentum flux layer and (b) the better choice of using the surface friction velocity in $K_{d,b}$ instead of a near-surface friction velocity, for estimating a near-surface dust flux with the FG method. Second, the short fetch of our plot may have also limited the development of a constant dust flux layer, although this could not be clearly demonstrated. In such a case, the higher FG dust sensor would have been located in the upper limit of the dust internal boundary layer developing from the upwind edge of the plot. This could explain some of the differences between the EC and FG transfer velocities for coarse particles during some event periods. Third, the hypothesis of similarity in turbulent transport between dust and momentum considered by the FG method in the calculation of $K_{d,b}$ ($\mathrm{Sc}_t = 1$) was not verified here due to the intermittency of dust emission as compared to the more continuous absorption of momentum by the surface. After correction of the FG fluxes, the difference and RMSE between the dust flux derived from both methods were reduced for coarse particles and April events.

This intercomparison highlights the difficulties and advantages of each method as well as their complementarity. The sampling head used for the EC method was limited to fine particles and requires (a) an improvement in order to cover the large size range of emitted dust particles, at least up to 10 μm, or (b) an accurate estimation of the EC dust concentration correction to cover larger particles, using at the same height an additional dust sensor with an appropriate sampling head for coarse particles. Above 10 μm, dust particles cannot be assumed to act as a gas, limiting the applicability of the EC method. The FG method still represents the only method able to cover the larger size range of the emission dust flux and to study the chemical composition of this flux, although (a) some corrections for the dissimilarity of the turbulent transport between momentum and dust may be needed and (b) the presence of the constant dust and momentum flux layers required by the method needs to be better verified in order to avoid erroneous interpretations. Dust fluxes estimated with the FG method have a smaller uncertainty than the dust fluxes from the EC method, the former method depending only on first order moments as opposed to second order moments for the EC method.

To conclude, the EC method is rarely applied in aeolian soil erosion research but its potential for estimating the size-resolved dust flux and importantly for understanding the mechanism of dust turbulent transport,

is promising, at the expense of improving the sampling head of the dust sensor under the constraint of not disturbing the sonic anemometer measurements. Compared to the FG method, the EC method allows in particular (a) to estimate a dust flux with less hypotheses and independent of the friction velocity and the thermal stability, avoiding self-correlation while afterward seeking for relationship between dust flux and these two variables, (b) to quantify the contribution of turbulent motions on dust transport following their size and how this contribution differs with the transport of other scalars (Dupont et al., 2019), and (c) to estimate the dust flux at very fine scales (from few minutes to few seconds) using the wavelet transform instead of the Fourier transform, revealing the role played by turbulence intermittency on dust emission (Dupont, 2020).

Appendix A: Uncertainty Estimation

Uncertainty on a mean quantity α, noted $\Delta[\alpha]$, is hereafter defined as the percentage of the standard deviation σ_α of α relative to α: $\Delta[\alpha] = \sigma_\alpha / \alpha$. This means that the 68.3% confidence interval of α is $\pm\Delta[\alpha]\alpha$.

A1. Uncertainty on the Size-Resolved FG Dust Flux

Three sources of uncertainty have been identified for the FG dust flux (Equation 7): (a) the surface friction velocity u_{*0}, (b) the difference of dust concentrations between the upper and lower levels $D\langle d_b\rangle = \langle d_b\rangle_{z_{up}} - \langle d_b\rangle_{z_{down}}$, and (c) the difference of stability between these two levels $D\Psi_m = \Psi_m\left(z_{down} / L\right) - \Psi_m\left(z_{up} / L\right)$. This leads to the following expression of the size-resolved uncertainty of F_b^{FG}:

$$\Delta\left[F_b^{FG}\right]^2 = \Delta\left[u_{*0}\right]^2 + \Delta\left[D\left\langle d_b\right\rangle\right]^2 + \Delta\left[D\Psi_m\right]^2 \tag{A1}$$

The uncertainties on u_{*0} and Ψ_m were estimated, respectively, equal as ±6% and ±2% in Dupont et al. (2018). The uncertainty on $D\Psi_m$ was then deduced as follows:

$$\Delta[a-b]^2 = \frac{\Delta[a]^2\left\langle a^2\right\rangle + \Delta[b]^2\left\langle b^2\right\rangle}{\left\langle a-b^2\right\rangle}, \tag{A2}$$

where $a = \Psi_m\left(z_{down} / L\right)$ and $b = \Psi_m\left(z_{up} / L\right)$, and $\langle\ \rangle$ refers to average quantity over the erosion event.

The uncertainty on $D\left\langle d_b\right\rangle$ was deduced per size class from the scatter (standard deviation) of the difference between the corrected dust concentrations of the two OPCs recorded during the intercomparison campaign, relative to the mean dust concentration.

A2. Uncertainty on the Size-Resolved EC Dust Flux

The estimation of the EC dust flux has three sources of uncertainty: (a) the sampling error $\Delta\left[S_{wd_b}\right]$ due to the limited number of independent samples contributing to the mean during the chosen averaging time T (15 min) (Businger, 1986), (b) the high frequency correction α_{HF} of the dust flux (Section 3.5), and (c) the corrected mean dust concentration $\alpha_d\left\langle d_b^{EC}\right\rangle$ (Section 3.4):

$$\Delta\left[F_b^{EC}\left(T\right)\right]^2 = \Delta\left[S_{wd_b}\left(T\right)\right]^2 + \Delta\left[\alpha_{HF}\right]^2 + \Delta\left[\alpha_b\left\langle d_b^{EC}\right\rangle\right]^2, \tag{A3}$$

where $\Delta\left[F_b^{EC}\left(T\right)\right]$ is the uncertainty of F_b^{EC} for each 15-min period.

The sampling error of the correlation $\left\langle w'd_b'\right\rangle$ during the period T is expressed as:

$$\Delta\left[S_{wd_b}\left(T\right)\right]^2 = \frac{\sigma_{w'd_b'}}{\left\langle w'd_b'\right\rangle}\sqrt{\frac{2\tau_{w'd_b'}}{T}}, \tag{A4}$$

where $\sigma_{w'd_b'}$ is the standard deviation of $w'_{d,b}$ and $\tau_{w'd_b'}$ is the integral time scale of $w'_{d,b}$ (scale of independent measure) (Kaimal & Finnigan, 1994). The integral time scale can be deduced either from the cospectrum peak or from the cross-correlation function, it is about 1.6 s here.

The uncertainty on $\alpha_b \left\langle d_b^{EC} \right\rangle$ was deduced per size class from (a) the standard deviation of the difference between the corrected dust concentrations of the EC OPC ($\alpha_d d_b^{EC}$) and the geometric mean dust concentration of the two FG OPCs (d_b^{FG}) recorded during the intercomparison campaign, and from (b) the uncertainty of the FG dust concentration:

$$\Delta\left[a\right]^2 = \frac{\Delta\left[a-b\right]^2\left\langle a-b^2\right\rangle - \Delta\left[b\right]^2\left\langle b^2\right\rangle}{\left\langle a^2\right\rangle} \tag{A5}$$

where $a = \alpha_d d_b^{EC}$ and $b = d_b^{FG}$, and $\langle\ \rangle$ refers to average quantity over the intercomparison campaign.

The uncertainty on the high frequency correction was estimated as ±1%.

Because $\Delta\left[S_{wd_b}\right]$ is time dependent, the average uncertainty $\Delta\left[F_b^{EC}\right]$ for each erosion event was deduced by averaging $\Delta\left[F_b^{EC}\left(T\right)\right]$ over each 15-min periods according to the intensity of the dust flux along the event:

$$\Delta\left[F_b^{EC}\right] = \sum_T \Delta\left[F_b^{EC}\left(T\right)\right] F_b^{EC}\left(T\right) / \sum_T F_b^{EC}\left(T\right). \tag{A6}$$

A3. Uncertainty on the Total FG and EC Dust Fluxes

The uncertainties on the total dust fluxes, including all particle sizes, in number and in mass, were estimated, respectively, as follows:

$$\Delta\left[F_{n,tot}^{\varphi}\right]^2 = \sum_b \left[\Delta\left[F_b^{\varphi}\right]^2 \left\langle F_b^{\varphi}\right\rangle^2\right] / \left\langle F_{n,tot}^{\varphi}\right\rangle^2, \tag{A7}$$

and

$$\Delta\left[F_{m,tot}^{\varphi}\right]^2 = \sum_b \left[\Delta\left[F_b^{\varphi}\right]^2 \left\langle F_b^{\varphi}\right\rangle^2 \left(\rho_p \pi \frac{d_{p,b}^3}{6}\right)^2\right] / \left\langle F_{m,tot}^{\varphi}\right\rangle^2, \tag{A8}$$

where φ is either FG or EC, and refers $\langle\ \rangle$ to average quantity over an erosion event.

Acknowledgments
The authors acknowledge the support of the French Research Agency (ANR) under the grant ANR-15-CE02-0013 (project WIND-O-V). The authors would like to thank: (a) Houcine Khatteli, Director of the Institut des Régions Arides (IRA) of Médenine, for the constant support of IRA in all research related to wind erosion, and in particular for giving us access to the Dar Dhaoui's experimental range and for the IRA's logistic help during the all experiment to ensure the success of the campaign, (b) the guards of the experimental stations (Noureddine Boukhli, Mokhtar Elghoul, and Mousbah Elghoul) for their constant help and surveillance of the experimental system, (c) Dr Mark R. Irvine and Christophe Chipeaux for their help with the data-acquisition setup from Raspberry PI, and (d) J. M. Bonnefond, S. Chevaillier, A. Feron, D. Garrigou, T. Henry-des-Tureaux, S. Sekrafi, and P. Zapf for their contribution to the field data collection. Finally, the authors thank J. A Gillies and two anonymous reviewer for their helpful comments.

Data Availability Statement

The processed data used in this study are available at the WIND-O-V Web site (https://www6.inra.fr/anr-windov/).

References

Aubinet, M., Grelle, A., Ibrom, A., Rannik, Ü., Moncrieff, J., Foken, T., et al. (1999). Estimates of the annual net carbon and water exchange of forests: The EUROFLUX methodology. *Advances in Ecological Research*, *30*, 113–175. https://doi.org/10.1016/s0065-2504(08)60018-5

Baldocchi, D. (2014). Measuring fluxes of trace gases and energy between ecosystems and the atmosphere - The state and future of the eddy covariance method. *Global Change Biology*, *20*, 3600–3609. https://doi.org/10.1111/gcb.12649

Berg, P., Reimers, C. E., Rosman, J. H., Huettel, M., Delgard, M. L., Reidenbach, M. A., & Özkan Haller, H. T. (2015). Technical note: Time lag correction of aquatic eddy covariance data measured in the presence of waves. *Biogeosciences*, *12*, 6721–6735. https://doi.org/10.5194/bg-12-6721-2015

Bonasoni, P., Cristofanelli, P., Calzolari, F., Bonafè, U., Evangelisti, F., Stohl, A., et al. (2004). Aerosol-ozone correlations during dust transport episodes. *Atmospheric Chemistry and Physics*, *4*, 1201–1215. https://doi.org/10.5194/acp-4-1201-2004

Businger, J. A. (1986). Evaluation of the accuracy with which dry deposition can be measured with current micrometeorological techniques. *Journal of Climate and Applied Meteorology*, *25*, 1100–1124. https://doi.org/10.1175/1520-0450(1986)025<1100:eotaww>2.0.co;2

Chou, C., Formenti, P., Maille, M., Ausset, P., Helas, G., Harrison, M., & Osborne, S. (2008). Size distribution, shape, and composition of mineral dust aerosols collected during the African Monsoon Multidisciplinary Analysis Special Observation Period 0: Dust and

Biomass-Burning Experiment field campaign in Niger, January 2006. *Journal of Geophysical Research*, *113*, D00C10. https://doi.org/10.1029/2008JD009897

Corrsin, S. (1975). Limitations of gradient transport models in random walks and in turbulence. *Advances in Geophysics*, *18*, 25–60. https://doi.org/10.1016/s0065-2687(08)60451-3

Csanady, G. T. (1963). Turbulent diffusion of heavy particles in the atmosphere. *Journal of the Atmospheric Sciences*, *20*, 201–208. https://doi.org/10.1175/1520-0469(1963)020<0201:tdohpi>2.0.co;2

Damay, P. E., Maro, D., Coppalle, A., Lamaud, E., Connan, O., Hébert, D., et al. (2009). Size-resolved eddy covariance measurements of fine particle vertical fluxes. *Journal of Aerosol Science*, *40*(12), 1050–1058. https://doi.org/10.1016/j.jaerosci.2009.09.010

Derbyshire, E. (2007). Natural minerogenic dust and human health. *Ambio*, *36*(1), 73–77. https://doi.org/10.1579/0044-7447(2007)36[73:nmdahh]2.0.co;2

Deventer, M. J., El-Madany, T., Griessbaum, F., & Klemm, O. (2015). One-year measurement of size-resolved particle fluxes in an urban area. *Tellus B: Chemical and Physical Meteorology*, *67*(1), 25531. https://doi.org/10.3402/tellusb.v67.25531

Deventer, M. J., Held, A., El-Madany, T. S., & Klemm, O. (2015). Size-resolved eddy covariance fluxes of nucleation to accumulation mode aerosol particles over a coniferous forest. *Agricultural and Forest Meteorology*, *214–215*, 328–340. https://doi.org/10.1016/j.agrformet.2015.08.261

Dorsey, J. R., Nemitz, E., Gallagher, M. W., Fowler, D., Williams, P. I., Bower, K. N., & Beswick, K. M. (2002). Direct measurements and parameterisation of aerosol flux, concentration and emission velocity above a city. *Atmospheric Environment*, *36*(5), 791–800. https://doi.org/10.1016/s1352-2310(01)00526-x

Dupont, S. (2020). Scaling of dust flux with friction velocity: Time resolution effects. *Journal of Geophysical Research: Atmospheres*, *125*(1), e2019JD031192. https://doi.org/10.1029/2019JD031192

Dupont, S., Rajot, J.-L., Labiadh, M., Bergametti, G., Alfaro, S. C., Bouet, C., et al. (2018). Aerodynamic parameters over an eroding bare surface: Reconciliation of the law of the wall and eddy-covariance determinations. *Journal of Geophysical Research: Atmospheres*, *123*, 4490–4508. https://doi.org/10.1029/2017JD027984

Dupont, S., Rajot, J.-L., Labiadh, M., Bergametti, G., Lamaud, E., Irvine, M. R., et al. (2019). Dissimilarity between dust, heat, and momentum turbulent transports during aeolian soil erosion. *Journal of Geophysical Research: Atmospheres*, *124*, 1064–1089. https://doi.org/10.1029/2018JD029048

Evan, A. T., Flamant, C., Fiedler, S., & Doherty, O. (2014). An analysis of aeolian dust in climate models. *Geophysical Research Letters*, *41*(16), 5996–6001. https://doi.org/10.1002/2014GL060545

Fernandes, R., Dupont, S., & Lamaud, E. (2020). Origins of turbulent transport dissimilarity between dust and momentum in semiarid regions. *Journal of Geophysical Research: Atmospheres*, *125*, e2019JD031247. https://doi.org/10.1029/2019jd031247

Foken, T. (2017). *Micrometeorology* (p. 362). Springer.

Foken, T., Göockede, M., Mauder, M., Mahrt, L., Amiro, B., & Munger, W. (2004). Post-field data quality control. In X. Lee, W. Massman, & B. Law (Eds.), Handbook of micrometeorology: A guide for surface flux measurements and analysis (Vol. 29, pp. 181–208). Springer.

Frangi, J.-P., & Richard, D. C. (2000). The WELSONS experiment: Overview and presentation of first results on the surface atmospheric boundary-layer in semiarid Spain. *Annales Geophysicae*, *18*, 365–384. https://doi.org/10.1007/s00585-000-0365-7

Fratini, G., Ciccioli, P., Febo, A., Forgione, A., & Valentini, R. (2007). Size-segregated fluxes of mineral dust from a desert area of northern China by eddy covariance. *Atmospheric Chemistry and Physics*, *7*(11), 2839–2854. https://doi.org/10.5194/acp-7-2839-2007

Garratt, J. R. (1990). The internal boundary layer—A review. *Boundary-Layer Meteorology*, *50*, 171–203. https://doi.org/10.1007/bf00120524

Gillette, D. A., Blifford, I. H., Jr., & Fenster, C. R. (1972). Measurements of aerosol size distributions and vertical fluxes of aerosols on land subject to wind erosion. *Journal of Applied Meteorology*, *11*, 977–987. https://doi.org/10.1175/1520-0450(1972)011<0977:moasda>2.0.co;2

Gillette, D. A., Marticorena, B., & Bergametti, G. (1998). Change in the aerodynamic roughness height by saltating grains: Experimental assessment, test of theory and operational parameterization. *Journal of Geophysical Research*, *103*(D6), 6203–6209. https://doi.org/10.1029/98jd00207

Högström, U. (1988). Non-dimensional wind and temperature profiles in the atmospheric surface layer: A re-evaluation. *Boundary-Layer Meteorology*, *42*, 55–78. https://doi.org/10.1007/bf00119875

Horst, T. W. (1997). A simple formula for attenuation of eddy fluxes measured with first-order-response scalar sensors. *Boundary-Layer Meteorology*, *82*, 219–233. https://doi.org/10.1023/a:1000229130034

Huneeus, N., Schulz, M., Balkanski, Y., Griesfeller, J., Prospero, J., Kinne, S., et al. (2011). Global dust model intercomparison in AeroCom phase I. *Atmospheric Chemistry and Physics*, *11*(15), 7781–7816. https://doi.org/10.5194/acp-11-7781-2011

Ishizuka, M., Mikami, M., Leys, J. F., Shao, Y., Yamada, Y., & Heidenreich, S. (2014). Power law relation between size-resolved vertical dust flux and friction velocity measured in a fallow wheat field. *Aeolian Research*, *12*, 87–99. https://doi.org/10.1016/j.aeolia.2013.11.002

Kaimal, J. C., & Finnigan, J. J. (1994). *Atmospheric boundary layer flows: Their structure and measurements* (p. 289). Oxford University Press.

Kaimal, J. C., Wyngaard, J. C., Izumi, Y., & Coté, O. R. (1972). Spectral characteristics of surface-layer turbulence. *Quarterly Journal of the Royal Meteorological Society*, *98*, 563–589. https://doi.org/10.1002/qj.49709841707

Khalfallah, B., Bouet, C., Labiadh, M. T., Alfaro, S. C., Bergametti, G., Marticorena, B., et al. (2020). Influence of atmospheric stability on the size-distribution of the vertical dust flux measured in eroding conditions over a flat bare sandy field. *Journal of Geophysical Research*, *124*, e2019JD031185. https://doi.org/10.1029/2019JD031185

Knippertz, P., & Todd, M. C. (2012). Mineral dust aerosols over the Sahara: Meteorological controls on emission and transport and implications for modeling. *Reviews of Geophysics*, *50*, RG1007. https://doi.org/10.1029/2011RG000362

Loubet, B., Cellier, P., Fléchard, C., Zurfluh, O., Irvine, M., Lamaud, E., et al. (2013). Investigating discrepancies in heat, CO_2 fluxes and O_3 deposition velocity over maize as measured by the eddy-covariance and the aerodynamic gradient methods. *Agricultural and Forest Meteorology*, *169*, 35–50. https://doi.org/10.1016/j.agrformet.2012.09.010

Mahowald, N. (2011). Aerosol indirect effect on biogeochemical cycles and climate. *Science*, *334*(6057), 794–796. https://doi.org/10.1126/science.1207374

Mahowald, N., Albani, S., Kok, J. F., Engelstaeder, S., Scanza, R., Ward, D. S., & Flanner, M. G. (2014). The size distribution of desert dust aerosols and its impact on the Earth system. *Aeolian Research*, *15*, 53–71. https://doi.org/10.1016/j.aeolia.2013.09.002

Mårtensson, E. M., Nilsson, E. D., Buzorius, G., & Johansson, C. (2006). Eddy covariance measurements and parameterisation of traffic related particle emissions in an urban environment. *Atmospheric Chemistry and Physics*, *6*, 769–785. https://doi.org/10.5194/acp-6-769-2006

Marticorena, B., Kardous, M., Bergametti, G., Callot, Y., Chazette, P., Khatteli, H., et al. (2006). Surface and aerodynamic roughness in arid and semiarid areas and their relation to radar backscatter coefficient. *Journal of Geophysical Research*, *111*, F03017. https://doi.org/10.1029/2006JF000462

Monin, A. S., & Obukhov, A. M. (1954). Basic laws of turbulent mixing in the ground layer of the atmosphere. *Trudy Geofiz, Instituta Akademii Nauk, SSSR*, *24*(151), 163–187.

Nickling, W. G., & Gillies, J. A. (1993). Dust emission and transport in Mali, West Africa. *Sedimentology*, *40*, 859–868. https://doi.org/10.1111/j.1365-3091.1993.tb01365.x

Oncley, S. P., Friehe, C. A., Larue, J. C., Businger, J. A., Itsweire, E. C., & Chang, S. S. (1996). Surface-layer fluxes, profiles, and turbulence measurements over uniform terrain under near-neutral conditions. *Journal of the Atmospheric Sciences*, *53*(7), 1029–1044. https://doi.org/10.1175/1520-0469(1996)053<1029:slfpat>2.0.co;2

Owen, P. R. (1964). Saltation of uniform grains in air. *Journal of Fluid Mechanics*, *20*, 225–242. https://doi.org/10.1017/s0022112064001173

Pendergrass, W., & Arya, S. P. S. (1984). Dispersion in neutral boundary layer over a step change in surface roughness—I. Mean flow and turbulence structure. *Atmospheric Environment*, *18*(7), 1267–1279. https://doi.org/10.1016/0004-6981(84)90037-4

Porch, W. M., & Gillette, D. A. (1977). A comparison of aerosol and momentum mixing in dust storms using fast-response instruments. *Journal of Applied Meteorology*, *16*, 1273–1281. https://doi.org/10.1175/1520-0450(1977)016<1273:acoaam>2.0.co;2

Raupach, M. R. (1991). Saltation layers, vegetation canopies and roughness lengths. *Acta Mechanica*, *1*, 83–96. https://doi.org/10.1007/978-3-7091-6706-9_5

Raupach, M. R., & Legg, B. J. (1984). The uses and limitations of flux-gradient relationships in micrometeorology. *Agricultural Water Management*, *8*, 119–131. https://doi.org/10.1016/0378-3774(84)90049-0

Shao, Y. (2008). Physics and modelling of wind erosion (2nd revised and expanded ed., Vol. 37). Springer.

Shao, Y., Ishizuka, M., Mikami, M., & Leys, J. F. (2011). Parameterization of size-resolved dust emission and validation with measurements. *Journal of Geophysical Research: Atmospheres*, *116*, D08203. https://doi.org/10.1029/2010JD014527

Shao, Y., Wyrwoll, K.-H., Chappell, A., Huang, J., Lin, Z., McTainsh, G. H., et al. (2011). Dust cycle: An emerging core theme in Earth system science. *Aeolian Research*, *2*(4), 181–204. https://doi.org/10.1016/j.aeolia.2011.02.001

Sow, M., Alfaro, S. C., Rajot, J. L., & Marticorena, B. (2009). Size resolved dust emission fluxes measured in Niger during 3 dust storms of the AMMA experiment. *Atmospheric Chemistry and Physics*, *9*(12), 3881–3891. https://doi.org/10.5194/acp-9-3881-2009

Stull, R. B. (1988). *An introduction to boundary layer meteorology* (p. 666). Kluwer Academic Publishers.

Textor, C., Schulz, M., Guibert, S., Kinne, S., Balkanski, Y., Bauer, S., et al. (2006). Analysis and quantification of the diversities of aerosol life cycles within AeroCom. *Atmospheric Chemistry and Physics*, *6*, 1777–1813. https://doi.org/10.5194/acp-6-1777-2006

Todd, M. C., Bou Karam, D., Cavazos, C., Bouet, C., Heinold, B., Baldasano, J. M., et al. (2008). Quantifying uncertainty in estimates of mineral dust flux: An intercomparison of model performance over the Bodélé Depression, northern Chad. *Journal of Geophysical Research*, *113*, D24107. https://doi.org/10.1029/2008JD010476

Uno, I., Wang, Z., Chiba, M., Chun, Y. S., Gong, S. L., Hara, Y., et al. (2006). Dust model intercomparison (DMIP) study over Asia: Overview. *Journal of Geophysical Research*, *111*(D12), D12213. https://doi.org/10.1029/2005JD006575

Wang, G., Zheng, X., & Tao, J. (2017). Very large scale motion and PM10 concentration in a high-Re boundary Layer. *Physics of Fluids*, *29*(6). https://doi.org/10.1063/1.4990087

Yin, Y., Wurzler, S., Levin, Z., & Reisin, T. G. (2002). Interactions of mineral dust particles and clouds: Effects on precipitation and cloud optical properties. *Journal of Geophysical Research*, *107*(D23), 4724. https://doi.org/10.1029/2001JD001544

Yu, H., Chin, M., Yuan, T., Bian, H., Remer, L. A., Prospero, J. M., et al. (2015). The fertilizing role of African dust in the Amazon rainforest: A first multiyear assessment based on data from Cloud-Aerosol Lidar and Infrared Pathfinder Satellite Observations. *Geophysical Research Letters*, *42*(6), 1984–1991. https://doi.org/10.1002/2015gl063040